

1 Unraveling Pathways of Elevated Ozone Induced by the 2020 2 Lockdown in Europe by an Observationally Constrained Regional 3 Model using TROPOMI

4 Amir H. Souri^{1*}, Kelly Chance¹, Juseon Bak², Caroline R. Nowlan¹, Gonzalo González Abad¹,
5 Yeonjin Jung¹, David C. Wong³, Jingqiu Mao^{4,5}, and Xiong Liu¹

6 ¹Atomic and Molecular Physics (AMP) Division, Harvard–Smithsonian Center for Astrophysics, Cambridge, MA,
7 USA

8 ²Institute of Environmental Studies, Pusan National University, Busan, South Korea

9 ³U.S. Environmental Protection Agency, Center for Environmental Measurement & Modeling, Research Triangle
10 Park, NC, USA

11 ⁴Geophysical Institute, University of Alaska Fairbanks, Fairbanks, AK, USA

12 ⁵Department of Chemistry and Biochemistry, University of Alaska Fairbanks, Fairbanks, AK, USA

13 * Corresponding author: ahsouri@cfa.harvard.edu

14

15 **Abstract.** Questions about how emissions are changing during the COVID-19 lockdown
16 periods cannot be answered by observations of atmospheric trace gas concentrations alone, in part
17 due to simultaneous changes in atmospheric transport, emissions, dynamics, photochemistry, and
18 chemical feedback. A chemical transport model simulation benefiting from a multi-species
19 inversion framework using well-characterized observations should differentiate those influences
20 enabling to closely examine changes in emissions. Accordingly, we jointly constrain NO_x and
21 VOC emissions using well-characterized TROPOMI HCHO and NO₂ columns during the months
22 of March, April, and May 2020 (lockdown) and 2019 (baseline). We observe a noticeable decline
23 in the magnitude of NO_x emissions in March 2020 (14-31%) in several major cities including Paris,
24 London, Madrid, and Milan expanding further to Rome, Brussels, Frankfurt, Warsaw, Belgrade,
25 Kyiv, and Moscow (34-51%) in April. However, NO_x emissions remain at somewhat similar
26 values or even higher in some portions of the UK, Poland, and Moscow in March 2020 compared
27 to the baseline possibly due to the timeline of restrictions. Comparisons against surface monitoring
28 stations indicate that the constrained model underrepresents the reduction in surface NO₂. This
29 underrepresentation correlates with the TROPOMI frequency impacted by cloudiness. During the
30 month of April, when ample TROPOMI samples are present, the surface NO₂ reductions occurring
31 in polluted areas are described fairly well by the model (model: -21±17%, observation: -29±21%).

32 **The observational constraint on VOC emissions is found to be generally weak except for lower**

33 **latitudes**. Results support an increase in surface ozone during the lockdown. In April, the
34 constrained model features a reasonable agreement with maximum daily 8 h average (MDA8)
35 ozone changes observed at the surface ($r=0.43$), specifically over central Europe where ozone
36 enhancements prevail (model: $+3.73\pm 3.94\%$, $+1.79$ ppbv, observation: $+7.35\pm 11.27\%$, $+3.76$
37 ppbv). The model suggests that physical processes (dry deposition, advection, and diffusion)
38 decrease MDA8 surface ozone in the same month on average by -4.83 ppbv, while ozone
39 production rates dampened by largely negative $J_{\text{NO}_2}[\text{NO}_2]-k_{\text{NO}+\text{O}_3}[\text{NO}][\text{O}_3]$ become less negative,
40 leading ozone to increase by $+5.89$ ppbv. Experiments involving fixed anthropogenic emissions
41 suggest that meteorology contributes to 42% enhancement in MDA8 surface ozone over the same
42 region with the remaining part (58%) coming from changes in anthropogenic emissions. Results
43 illustrate the capability of satellite data of major ozone precursors to help atmospheric models
44 capture ozone changes induced by abrupt emission anomalies.

45 **1. Introduction**

46 Continuous monitoring of air pollution by satellites can help our understanding of both
47 anthropogenic and biogenic variability and change caused by rapid economic recession
48 [Castellanos and Boersma, 2012] and regulations [Krotkov et al., 2016; Souri et al., 2020a]. Earth's
49 atmosphere has substantially become more polluted since the industrial era in comparison to its
50 original environmental condition [Li and Lin, 2015], thus any abrupt hiatus in anthropogenic (man-
51 made) emissions should result in an immediate impact on relatively short lifetime pollutants such
52 as nitrogen dioxide (NO_2), formaldehyde (HCHO), and tropospheric ozone (O_3). The beginning of
53 the global COVID-19 pandemic in early 2020 [Fauci et al., 2020] provided such an abrupt change
54 in human activities [Le Quéré et al., 2020]. A first step to fully understand how much of these
55 impacts are related to the pandemic lockdowns is to disentangle the **physiochemical** processes
56 determining their ambient concentrations. Unraveling those processes require precise, continuous
57 observations of physical and chemical states and emission rates, which are not routinely available
58 on global, continental and regional scales. Therefore, we resort to using a model realization
59 attempting to reproduce such an intricate system. Models without observational guidance are
60 incapable of numerically representing the real world [Lorenz, 1963], so our best option to improve
61 a model is to constrain some of its prognostic inputs using well-characterized observations.
62 Accordingly, the framework of this study is centered around inverse modeling and data
63 assimilation.

64 Significant attention has been given to documenting the lockdown-related changes in
65 atmospheric composition around the world using both in-situ and satellite observations [e.g.,
66 Sicard et al., 2020; Shi and Brasseur, 2020; Lee et al., 2020; Salma et al., 2020; Le Quéré et al.,
67 2020; He et al., 2020; Le et al., 2020; Miyazaki et al., 2020; Liu et al., 2020; Barré et al., 2020;
68 Goldberg et al., 2020; Ordóñez et al., 2020; Wyche et al., 2021; Bekbulat et al., 2020; Gaubert et
69 al., 2021; Sun et al., 2021]. The broad picture is consistent among these studies; the lockdown
70 drastically reduced the concentrations of NO_x, CO, and SO₂ and some types of particulate matter,
71 whereas the concentrations of several secondarily formed compounds such as ozone behaved in
72 non-linear ways due to emissions and/or meteorology.

73 The motivations of this study are to determine the capability of a regional model
74 constrained by satellite HCHO and NO₂ columns to capture near-surface pollution, and if local
75 ozone production rates are the driving factors for heightening ozone pollution during the 2020
76 lockdown. In other words, what **physiochemical** processes are associated with the elevated ozone?
77 How representative are satellite observations at capturing surface air quality through an inversion
78 context? Is meteorology the primary factor in shaping elevated ozone as suggested by Ordóñez et
79 al. [2020]?

80 To address these pivotal questions, it is desirable to constrain models using multi-species
81 observations because relationships between the atmospheric compounds such as HCHO and NO₂
82 are importantly intertwined [Marais et al., 2012; Valin et al., 2016; Wolfe et al., 2016; Souri et al.,
83 2020a,b]. Accordingly we build our inversion framework upon a non-linear joint analytical
84 inversion of NO_x and VOCs proposed in Souri et al. [2020a] using the TROPospheric Monitoring
85 Instrument (TROPOMI) HCHO and NO₂ observations in Europe. Performing this type of
86 inversion not only enables us to precisely quantify **the changes in** emissions (along with its
87 uncertainty, as the inversion framework is analytical) but also paves the way for estimating the
88 resulting changes on different pathways of ozone.

89 **2. Measurements, Modeling, and Methods**

90 ***2.1. Satellite Observations***

91 *2.1.1. TROPOMI NO₂*

92 We use daily offline S5P TROPOMI tropospheric NO₂ slant columns
93 [Copernicus Sentinel data processed by ESA and Koninklijk Nederlands
94 Meteorologisch Instituut (KNMI), 2019] derived from a two-step framework

95 involving DOAS spectral fitting in conjunction with a stratosphere/troposphere
96 decoupler [Boersma et al., 2018]. The time periods of this study are March, April,
97 and May 2020 and 2019. The data provide Jacobians of light intensity with respect
98 to optical thickness (i.e., vertically-resolved scattering weights) which are
99 dependent on scene surface reflectivity, the cloudiness of the assumed Lambertian
100 clouds, and the sensor viewing geometry.

101 Aerosol effects on the scattering weights are not taken into consideration.
102 Based on radiative transfer calculations and satellite-based aerosol products, Jung
103 Y. et al [2019] and Cooper et al. [2019] observed small changes (<10%) in AMFs
104 with and without considering the aerosol impacts in Europe in springtime. This
105 tendency likely results from a low aerosol optical depth.

106 The 2019 TROPOMI observations used in this study have a spatial
107 resolution of $7 \times 3.5 \text{ km}^2$, whereas those in 2020 have a spatial resolution of 5.5×3.5
108 km^2 . The NO₂ products for the study time period were produced by processor
109 versions v01.02.02 (1 March 2019 – 20 March 2019) and v01.03.02 (20 March
110 2019 onward). The v01.03.02 processor includes an update to the FRESCO-S cloud
111 algorithm and improvements to a quality flag variable. NO₂ validation from
112 processors v01.02.02 and v01.03.02 shows similar biases and dispersion [Lambert
113 et al., 2020], as do comparisons from before and after the pixel spatial resolution
114 change [Verhoelst et al., 2021]. We extract good quality pixels based on the main
115 quality flag (`qa_flag`) > 0.75, which removes retrievals flagged as bad and pixels
116 over snow/ice or with cloud radiance fractions > 0.5, and resample them to our 15-
117 km regional model (discussed later) using the bilinear interpolation. Since vertical
118 column densities (VCDs) depend on assumed gas profile shape (i.e., they are quasi-
119 observations), we recalculate those shape factors using profiles from our
120 constrained chemical transport model. Shape factors are re-estimated by calculating
121 the ratio of the vertical column of total air to the simulated vertical column of NO₂
122 multiplied by the mixing ratios of NO₂ profile from the regional model [Martin et
123 al., 2002].

124 Satellite remote sensing observations are usually far more stable than they
125 are accurate. This can make the data practical for measuring relative changes in

126 emissions, but may necessitate the use of a bias correction for absolute emissions
127 estimates. Moreover, the systematic and random errors associated with satellite
128 retrievals may differ markedly from location to location. It is therefore crucial to
129 thoroughly validate columns against independent observations. To this end, we
130 compile statistics reported in several validation studies focusing on the TROPOMI
131 tropospheric NO₂ product and summarize their findings in Table 1. The most
132 comprehensive global study to date is a comparison of TROPOMI tropospheric
133 NO₂ with that derived from 19 MAX-DOAS instruments [Verhoelst et al., 2021].
134 This study indicates there is a low bias in TROPOMI tropospheric NO₂ of -23 to -
135 37% relative to MAX-DOAS at clean to moderately polluted sites, and as large as
136 -51% at highly polluted sites. When considering all sites, the overall median bias
137 in this study was found to be -37%, with a dispersion of 3.5×10^{15} molec/cm²
138 (defined as half of the 68% interpercentile). No obvious seasonal patterns were
139 found in the biases. These results are consistent with other validation studies which
140 have observed a low bias in TROPOMI tropospheric NO₂ [Chan et al., 2020; Griffin
141 et al., 2019; Judd et al., 2020]. A potential significant source of bias in polluted
142 regions is the relatively low spatial resolution ($1 \times 1^\circ$) TM5-MP prior profiles used
143 in the TROPOMI air mass factor calculation. Several validation studies have shown
144 the low bias in TROPOMI NO₂ can be reduced in polluted regions by 5-17%
145 through the use of higher spatial resolution model a priori profiles or other
146 improvements in the AMF calculation [Chan et al., 2020; Griffin et al., 2019; Judd
147 et al., 2020; Zhao et al., 2020].

148 Directly incorporating these numbers into an inversion model is
149 challenging, mainly because of spatiotemporal variability in the satellite errors.
150 Ideally, the relationship between errors and retrieval inputs (e.g., albedo, scene
151 radiance, profiles, etc.) would be used as an additional cost function in the
152 inversion, commonly known as variational bias correction [e.g., Auligné et al.,
153 2007]. In the absence of such relationships, we use the biases reported in the
154 validation studies.

155 In the case of NO₂, we uniformly scale up the satellite tropospheric columns
156 by 25%. This bias estimate is derived by first assuming a 37% low bias in the

157 columns over polluted regions as reported by Verhoelst et al. [2021]. In turn, this
 158 low bias can be mitigated somewhat by the application of high spatial resolution
 159 profiles in the air mass factor calculation, such as the ones used in this study. Table
 160 1 summarizes the results from several TROPOMI validation studies at specific
 161 locations that calculated NO₂ using model profiles with higher spatial resolution
 162 than the operational TROPOMI (1°×1°) profiles (see Table 1 columns
 163 “Modification” and “Modified Bias”). In these studies, modified columns show
 164 increases ranging from 0 - 25%. Based on these results, we assume a low bias of
 165 37% can be mitigated by ~12% through the use of high spatial resolution profiles,
 166 for a resulting total low bias of 25%. This bias is likely not valid over pristine areas,
 167 where validation studies show lower biases in TROPOMI NO₂ [Verhoelst et al.,
 168 2021, Wang et al., 2020, Zhao et al., 2020]; nonetheless, we previously observed
 169 in Souri et al. [2020a] that the low signal-to-noise ratios of those column amounts
 170 resulted in small changes in the top-down emissions. We assume the errors of
 171 observations originate from two main sources: i) the precision error provided with
 172 the data ($e_{\text{precision}}$) and ii) a fixed error estimated from comparisons to in-situ
 173 measurements (e_{const}). Mathematically, the final error is:

$$e_o^2 = e_{\text{const}}^2 + \frac{1}{n^2} \sum_{i=1}^n e_{\text{precision},i}^2 \quad (1)$$

174 where n is the number of samples for a given grid and e_{const} equals to 1.1×10^{15}
 175 molec/cm² ($< 6 \times 10^{15}$ molec/cm²) in clean regions and 3.5×10^{15} molec/cm²
 176 ($\geq 6 \times 10^{15}$ molec/cm²) in moderately to highly polluted regions. These regions are
 177 defined based on the wide ranges reported in Verhoelst et al. [2021] ($3\text{-}14 \times 10^{15}$
 178 molec/cm² for moderately to highly polluted regions).

2.1.2. MODIS AOD

180 To improve the simulation of total aerosol mass, we use the collection 6
 181 MODIS aerosol optical depth (AOD) from both Aqua (~ 13:30 LT) and Terra (~
 182 10:30 LT) platforms over both land and ocean [Levy et al., 2013] (available at
 183 <https://ladsweb.modaps.eosdis.nasa.gov>, access May 2020). We independently
 184 validate all three major products, namely the deep blue, the dark target and a
 185 combined dark blue products by comparing to AOD values measured by

186 AERONET over Europe at the same time period of this study. Only good and very
187 good ($qa \geq 2$) pixels are selected for the comparison. The AERONET AOD data
188 are computed based on the values at 500 nm and Angstrom Exponent in the 440-
189 675 nm range. We collocate two datasets if they are within 10 km radius and less
190 than 30 mins apart. The dark blue product results in the best agreement ($r > 0.87$)
191 with a high bias of < 0.05 (Figure S3, and S4). This product is therefore chosen for
192 the data assimilation. We remove the bias and assign the value of the covariance
193 matrix of observations to the RMSE values obtained from the comparison.

194 **2.2. Surface Measurements**

195 UV photometry and chemiluminescence surface ozone and NO_2 measurements all
196 over continental Europe are used to investigate possible changes in their concentrations
197 induced by the lockdown (<https://discomap.eea.europa.eu/map/fme/AirQualityExport.htm>,
198 access June 2020). The NO_2 chemiluminescence measurements are usually overestimated
199 due to interferences from the NO_z family (PAN, organic nitrate, HNO_3 , etc.). We assume
200 that the interferences are not significantly different between the baseline and lockdown
201 mainly due to relatively low photochemistry in early spring [Lamsal et al., 2008] compared
202 to summertime. Additionally, the correction needs a careful evaluation of the model with
203 regards to the NO_z family whose measurements are not available in this case study.

204 More than 6450 meteorological stations archived on NOAA's integrated surface
205 database (<https://www.ncei.noaa.gov/data/global-hourly/>, access April 2020) are used to
206 validate the performance of our weather model in terms of several prognostic inputs
207 including ambient air temperature, air humidity, and U and V wind components.

208 **2.3. WRF-CMAQ Modeling**

209 The regional air quality simulations at $15 \times 15 \text{ km}^2$ are carried out with the widely
210 used CMAQ v5.2.1 (<https://doi.org/10.5281/zenodo.1212601>) in conjunction with WRF
211 v3.9.1 [Skamarock et al. 2008] models. The models overlap and cover continental Europe
212 and some portions of Africa and Middle East. The domain consists of 483 east-west, 383
213 north-south grids, and 37 unevenly spaced eta levels (Figure 1). The simulation time period
214 is from March to May 2019 and 2020 (six months). Since IC/BC are taken from already
215 spun-up National Centers for Environmental Prediction (NCEP) FNL (final) reanalysis and
216 GEOS-Chem v12.9.3 (10.5281/zenodo.3974569) runs, we only spin up the models for the

217 month of February. The chemistry configuration of the CMAQ model mainly consists of
218 CB05 with chlorine chemistry (gases) and AERO6 (aerosol). Hourly-basis biogenic
219 emissions are processed by the offline standalone Model of Emissions of Gases and
220 Aerosols from Nature (MEGAN) v2.1 model [Guenther et al., 2012] based on high-
221 resolution plant functional maps made by Ke et al. [2012]. The biogenic emission factors
222 are estimated based on the PFT-specific information provided in Guenther et al. [2012].
223 The biogenic VOCs include a wide range of compounds including isoprene, monoterpenes,
224 aromatic VOCs, and methanol. Soil NO_x emissions are estimated by Yienger and Levy,
225 [1999]. Lightning NO_x emissions are based on in-line calculations involving convective
226 precipitation rates and cloud vertical distributions. Lightning NO_x emissions are not
227 constrained in the model. Anthropogenic emissions are based on the Community Emissions
228 Data System (CEDS) inventory in 2014 [Hoesly et al., 2018]. Diurnal scales are not
229 considered for the anthropogenic emissions. We also output the CMAQ integrated process
230 analysis quantifying the contribution of each process to the amount of compounds. The
231 physical setting of WRF includes the Lin microphysics scheme [Lin et al., 1983], the Grell
232 3-D ensemble cumulus scheme [Grell and Dévényi, 2002], the RRTMG radiation scheme,
233 ACM2 planetary boundary layer parametrization [Pleim, 2007], and Pleim-Xu land-
234 surface scheme [Xiu and Pleim, 2001]. To minimize the deviation of the model from the
235 reanalysis data, we turn on the grid nudging option with respect to wind, moisture, and
236 temperature only outside of the PBL region. The inclusion of this option only outside of
237 the PBL region is because we do not want the coarse reanalysis data wash out the relatively
238 high-resolution dynamics. Moreover, leaf area index and the sea surface temperature are
239 updated every 6 hours based on satellite measurements included in the reanalysis data.
240 Extensive model evaluations based upon surface observations show a striking
241 correspondence (Table S1, S2) which is indicative of **reasonable** energy budget and
242 transport in our model.

243 ***2.4. Inverse Modeling and Data Assimilation***

244 To adjust the bottom-up emission inventories, we follow a non-linear joint
245 inversion method proposed in Souri et al. [2020a]. Briefly, a Gauss-Newton algorithm is
246 utilized to incrementally solve the Bayes' quadratic function in analytical fashion. The
247 posterior emissions are then derived by

$$\mathbf{x}_{i+1} = \mathbf{x}_a + \mathbf{G}[\mathbf{y} - F(\mathbf{x}_i) + K_i(\mathbf{x}_i - \mathbf{x}_a)] \quad (2)$$

248 where \mathbf{y} is bias-corrected monthly-averaged TROPOMI NO₂ and HCHO observations (see
 249 S.A1), \mathbf{x}_a (or \mathbf{x}_0) is the prior emissions, \mathbf{x}_i is the posterior emission at the i th increment, F
 250 is the forward model (here WRF-CMAQ) to project the emissions onto columns space, \mathbf{G}
 251 is the Kalman gain,

$$\mathbf{G} = \mathbf{S}_e K_i^T (K_i \mathbf{S}_e K_i^T + \mathbf{S}_o)^{-1} \quad (3)$$

252 and $K_i (= K(\mathbf{x}_i))$ is the Jacobian matrix calculated explicitly from the model using the finite
 253 difference method by perturbing separately NO_x and VOC emissions by 20%. The
 254 perturbations are applied for each iteration. The model outputs along with Jacobians and
 255 emissions are spatiotemporally co-registered with the observations. \mathbf{S}_o and \mathbf{S}_e are the error
 256 covariance matrices of the observations and emissions. Similar to Souri et al. [2020a], the
 257 prior errors in anthropogenic NO_x and VOCs emissions are set to 50% and 150%,
 258 respectively. In terms of the biogenic emissions, the errors are set to 200% for both NO_x
 259 and VOCs. The instrument covariance matrices are populated with squared-sum of the
 260 aforementioned errors based on the compilation of the validation studies and precision
 261 errors provided with the data (Eq.1). Both error matrices are assumed diagonal. The
 262 inversion window is monthly meaning we have three separate correction factors in months
 263 of March, April, and May. The covariance matrix of the a posteriori is calculated by:

$$\hat{\mathbf{S}}_e = (\mathbf{I} - \mathbf{G}\hat{K}) \mathbf{S}_e \quad (4)$$

264 where \hat{K} is the Jacobian from the i th iteration. Here we iterate Eq.2 three times. The
 265 averaging kernels (\mathbf{A}) are given by:

$$\mathbf{A} = \mathbf{I} - \hat{\mathbf{S}}_e \mathbf{S}_e^{-1} \quad (5)$$

266 Not only does this method considers non-linear chemical feedback among NO₂-
 267 HCHO-NO_x-VOC by simultaneously incorporating the HCHO and NO₂ in the inversion
 268 framework, it also permits quantification of \mathbf{A} that explicitly explains the amount of
 269 information obtained from the observation. Low \mathbf{A} indicates low \mathbf{G} making the a posteriori
 270 to be rather independent of the observational constraint.

271 **An important caveat with this inversion system is that we do not take the model**
 272 **parameter error (such as errors in chemistry, cloud microphysics, and PBL) into account.**
 273 **To properly estimate the forward model parameter errors, one needs to calculate the**

274 sensitivity matrix of the columns to the model parameters combined with the sensitivity
275 matrix of the columns to the emissions (K) [Rodgers, 2000]. The former calculation is
276 computationally expensive. Moreover, the spatiotemporal varying model parameter errors
277 may not be known in detail. The consequence of disregarding the model parameter errors
278 is the overconfidence in the top-down estimates (i.e., overestimations of AKs).

279 We also correct total aerosol mass by daily assimilating the MODIS dark blue AOD
280 observations following the algorithm discussed in Jung et al. [2019]. Briefly, the
281 assimilation framework uses a modified optimal interpolation method adjusting uniformly
282 all relevant aerosol masses in a column as a function of a weighted-distance and appropriate
283 errors.

284 3. Results and Discussion

285 3.1. Variability of NO_2 columns seen by TROPOMI

286 We assess difference maps of NO_2 columns (and HCHO in S1) in 2020 with respect to
287 those in 2019 during the months of March, April and May. The difference maps along with the
288 absolute values of the tropospheric NO_2 columns are shown in Figure 2. Regardless of the year,
289 we observe a noticeable reduction in NO_2 as we approach warmer months which can be explained
290 by increases in OH concentrations (higher water vapor content, solar radiation, and O_3 levels),
291 faster vertical mixing due to larger sensible fluxes (more diluted columns for a given receptor due
292 having a greater chance of experiencing stronger winds in higher altitudes), and a reduction in
293 temperature-dependent light-duty diesel NO_x emissions [Grange et al., 2019]. This sequential
294 decline of NO_2 obscures the quantitative interpretation of the satellite observations in two ways:
295 first, as noted by Silvern et al. [2019], the free tropospheric background NO_2 levels, which are
296 highly uncertain, becomes comparable to those located at near-surface, and second, the relatively
297 lower signal-to-noise ratios reduce the amount of information that we can obtain for inverting NO_x
298 emissions (discussed later).

299 The anomaly map (2020 vs 2019) in March indicates pronounced decreases in tropospheric
300 NO_2 columns over several countries including France, Spain, Italy, and Germany (box A). In
301 contrast, we see increases in the magnitude of the NO_2 columns over some portions of the UK
302 excluding London (box B), northeastern Germany (box C), and Moscow, Russia (box D). A recent
303 study [Barré et al. 2020] observed roughly the same tendency which was attributable to
304 meteorological changes. While those changes are indeed an important piece of information, we

305 should recognize that the degree of the enforced restrictions varies temporally; moreover changes
306 in emission heavily rely on the dominant emission sector (e.g., mobile or industry). For instance,
307 according to TASS press [<https://tass.com/society/1144123>, accessed Sep 2020], Russian
308 governments did not take significant measures to control the virus before April 15, immediately
309 evident in the large NO₂ enhancement over Moscow in March (box D). During the next two months
310 (April and May), we observe a major turnaround over this city (box F and H). In May, the anomaly
311 of the tropospheric NO₂ suggests that the reduction in NO_x emissions abruptly experiences a hiatus
312 in central Europe (box G). However it is crucial to note that these maps are based upon sporadic
313 clear-sky pixels that might obscure the full portrayal of emissions changes happening throughout
314 the period (discussed later).

315 *3.2. Top-Down estimates of NO_x emissions*

316 Following the inversion and the data assimilation frameworks, we adjust the total amounts
317 of VOC, NO_x emissions, and aerosols mass using TROPOMI HCHO, NO₂ and MODIS AOD
318 observations. We focus on the topic of gas phase chemistry (i.e., ozone and its precursors) implying
319 that the aerosol data assimilation is carried out to partially remove errors associated with radiation
320 [e.g., Jung et al., 2019] or heterogenous chemistry [Jacob, 2000]; therefore, the aspect of aerosol
321 changes induced by the lockdown will be examined in a separate study. **Furthermore, we observe**
322 **a relatively weak observational constraint from TROPOMI HCHO on VOC emissions, especially**
323 **in higher latitudes; accordingly, the relevant discussion on this subject is presented in S2.**

324 The spatial distributions of magnitude of the top-down NO_x and their corresponding
325 changes and averaging kernels are shown in Figure 3. Moreover, the monthly values of the a
326 posteriori and the a priori are shown in Figure S5 and S6. It is worth emphasizing that we use
327 identical prior values in terms of anthropogenic emissions in both years.

328 According to Figure 3, large averaging kernels associated with NO_x emissions are confined
329 in high-emitting regions suggesting that the most valid estimates can be found in areas undergoing
330 strong TROPOMI NO₂ signals. We observe an improvement in the statistics associated with
331 simulated surface NO₂ using the posterior emissions compared to the surface measurements in
332 many places around Europe with an exception to northeastern Germany where TROPOMI NO₂
333 observations deviates the model from the measurements (Figs S9-S12; **Tables S3, S4**). **The large**
334 **underestimation of the model in terms of surface NO₂ concentrations is most likely due to the**
335 **underestimation of the CEDS inventory [e.g., Figure 11 in Sun et al., 2021]. However, it is worth**

336 noting that the disagreements between the model and the surface measurements do not solely
337 reflect the uncertainty in the emissions. A major complication arises from the fact that the point
338 measurements represent concentrations locally, whereas the model grids ($15 \times 15 \text{ km}^2$) are (at best)
339 the average of infinitesimal points integrated over the grid space. Essentially, no one should expect
340 that these quantities will completely line up, unless one transforms the point measurements to the
341 grids (i.e., rasterization) by carefully modeling the spatial auto-correlation (or semivariograms) of
342 the point data [Souri et al., 2021]. Additionally, there is uncertainty about the chemical mechanism
343 utilized in the model. In particular, Souri et al. [2017] observed a large overestimation (\sim factor 4)
344 of daily-averaged total nitrate ($\text{HNO}_3 + \text{NO}_3^-$) in the CB05/AERO6 mechanism despite moderately
345 reasonable nitrate (NO_3^-) simulations. This was attributed to a large overestimation of N_2O_5
346 hydrolysis rate [Bertram and Thornton, 2009] which is the primary loss pathway of NO_x in low
347 photochemically active regions [Shah et al., 2020]. The interferences from the NO_z family on the
348 surface measurements might be still present in springtime in midlatitudes ($\sim 10\text{-}30\%$) [Lamsal et
349 al., 2008]. Last but not the least, the PBL parameterization controlling the level of vertical mixing
350 rates has errors primarily due to soil moisture not being observationally constrained in the model
351 [Huang et al., 2021].

352 The discrepancies between the simulated tropospheric NO_2 columns versus TROPOMI are
353 mitigated by the inversion (Figure S13 and S14). Immediately apparent in Figure 3 is a strong
354 correlation between anomaly maps of TROPOMI tropospheric NO_2 (Figure 2) and those of top-
355 down emissions. We observe reductions in NO_x emissions in March (14-31%) in several major
356 cities including Paris, London, Madrid, and Milan; the reductions further expand to Rome,
357 Brussels, Frankfurt, Warsaw, Kyiv, Moscow, and Belgrade with higher magnitudes (34-51%) in
358 April. In general, the level of NO_x reduction is somewhat higher in April relative to months of
359 March and May possibly due to temporal variabilities associated with the restrictions; for example,
360 UK and Poland governments enforced the restrictions starting in the last week of March to the
361 middle of April (see Figure S1 in Okruszek et al. [2020]; <https://www.bbc.com/news/uk-51981653>, accessed in March 2020). The decreased anthropogenic NO_x emissions in the strait of
362 Gibraltar and Alboran Sea reveal reportedly reduced ship activities [United Nations Conference
363 on Trade and Development Report, Accessed Dec 2020]. The numbers in May indicate that several
364 countries in central and eastern Europe (shown in box G in Figure 2) likely eased coronavirus
365

366 lockdown restrictions, a picture that has yet to be verified by surface measurements (discussed
367 later).

368 **3.3. Disparities in near-surface concentrations suggested by the constrained model versus** 369 **those by in-situ measurements**

370 **3.3.1. NO_2**

371 It is necessary to examine whether the constrained model can precisely represent the
372 changes observed by surface measurements. Several factors can complicate this analysis: i) having
373 overconfidence in the constrained model where the satellite observations used were uncertain; this
374 problem can be addressed by considering grid cells whose averaging kernels are above a threshold
375 (here 0.5), ii) not accounting for spatial representativity function when it comes to directly
376 comparing two datasets at different scales (i.e., point measurements vs the model grids); a
377 statistical construction of the spatial representivity function [Janic et al., 2016; Souri et al., 2021]
378 requires a dense observational network so that we can build a semivariogram; instead, we only
379 consider model grid cells having more than two stations; those observations then are then averaged,
380 iii) interferences of the NO_z family on NO_2 chemiluminescence measurements [Dickerson et al.,
381 2019] which can be partly discounted when calculating differences, iv) model uncertainties,
382 especially with respect to turbulent and convective fluxes that are heavily determined by
383 representing local heterogeneity of forces and non-hydrostatic dynamics [Emanuel, 1994], all of
384 which are challenging to fully resolve in a 15-km resolution.

385 With these caveats in mind, we plot the daily-averaged changes of surface NO_2
386 concentrations in 2020 relative to 2019 derived by the model and the European air quality network
387 for the months of March, April, and May (Figure 4). Large gaps in Figure 4 are caused by
388 considering grid cells with averaging kernels >0.5 and number of samples >2 . The constrained
389 model correlates reasonably well with the changes observed by the surface **measurements in April**,
390 but it fails to **fully** reflect those in **March and May**. The surface measurements in March reinforce
391 increases (or negligible changes) in NO_2 in northeastern Germany and UK, although the
392 magnitudes are not as large as those suggested by the model (**and TROPOMI NO_2 columns**). **A**
393 **number of factors can contribute to these large discrepancies:** i) the surface measurements were
394 **present throughout the month of March, whereas TROPOMI data were frequently absent due to**
395 **cloudiness resulting in some degree of temporal representativity issues;** ii) the statistics used for
396 **the TROPOMI bias-correction may not always hold true, since each individual pixel can deviate**

397 from the norm of the reported biases; iii) the shape of NO₂ profiles simulated by the WRF-CMAQ
398 can sometimes be uncertain due to errors in the PBL parameterization or the difficulties with
399 resolving the non-hydrostatic components (where vertical motions are comparable to horizontal
400 ones) [e.g., Pouyaei et al., 2021]; this complication can result in unrealistic changes in the columns.
401 The constrained model tends to consistently underrepresent the decline in NO₂ in March (model:
402 -11±21%, observation: -19±16%), April (model: -21±17%, observation: -29±21%), and May
403 (model: -12±18%, observation: -25±20%). The frequency of TROPOMI data heavily impacted by
404 cloudiness is an important factor effectively leading to the underrepresentation of the model in a
405 course of a month. Figure 5 depicts the average number of days that TROPOMI was able to sample
406 on in both years (individual years are shown in Figure S18 and S19). There is a strong degree of
407 correlation between the frequency of the data and the discrepancy between the model versus the
408 surface observations. This is especially the case for May when we see too few days to be able to
409 realistically reproduce NO₂ changes.

410 Given the reasonable performance of our model at reproducing the changes observed over
411 the surface in April, a result of abundant samples from TROPOMI, we only focus on this month
412 for the subsequent analysis.

413 3.3.2. *Ozone*

414 Figure 6 depicts the changes in maximum daily 8 h average (MDA8) surface ozone
415 concentrations suggested by the measurements and the constrained model in April 2020 with
416 respect to 2019. Immediately obvious from the observations is the elevated surface ozone
417 concentrations up to 32% in places where NO_x emissions drastically decreased such as Germany,
418 Italy, France, UK, Switzerland, and Belgium (shown as box L). This tendency potentially driven
419 by ozone chemistry [Sicard et al., 2020a; Shi and Brasseur, 2020; Grange et al. 2020; Salma et al.,
420 2020; Lee et al., 2020] and/or meteorology [Lee et al., 2020; Wyche et al., 2021; Ordóñez et al.,
421 2020] has drawn much attention. The challenge is to set up a model that is the characteristic of
422 such a complex tendency [e.g., Parrish et al., 2014]. Encouragingly, our constrained model does
423 have skill in describing the ozone enhancements over the whole domain ($r=0.43$). In the proximity
424 of central Europe (shown as box L), the enhanced MDA8 ozone concentration observed by the
425 observations is 7.35±11.27% (+3.76 ppbv) which is nearly a factor of two larger than that of the
426 model (3.73±3.94%, +1.79 ppbv).

427 We plot the simulated MDA8 surface ozone concentrations in April 2020 (lockdown),
428 April 2019 (baseline), and their differences in Figure 7. Surface ozone concentrations show a
429 strong latitudinal gradient with lower values in higher latitudes, underscoring the importance role
430 of solar radiation in the formation of ozone. Meanwhile, the Mediterranean basin is prone to
431 elevated concentrations of ozone resulting from different factors including calm weather, the
432 transport from neighboring countries, atmospheric recirculation in coastal environments, and local
433 emissions [Lelieveld et al., 2002]. While we observe a strong variability in the difference map,
434 signaling various sources and sinks (discussed later), three distinctive features in 2020 in
435 comparison to 2019 are evident: i) higher concentrations over the central Europe (up to 5 ppbv),
436 ii) lower concentrations in eastern Europe (-2.67 ± 1.65 ppbv) due to the 2019 biomass burning
437 activities (see S1 and S2) and larger snow cover fraction accelerating photolysis [e.g.,
438 Rappenglück et al., 2014], and iii) lower values in the Iberian Peninsula (-0.51 ± 1.41 ppbv)
439 [Ordóñez et al., 2020].

440 While the remaining model uncertainty could be either improved or characterized by
441 including more observations (if available), reconfiguring the **physiochemical** mechanisms used,
442 and constraining chemical boundary conditions, it is imperative to gauge the contribution of each
443 process (i.e., transport, chemistry, etc.) in forming ozone changes. Here we mainly make use of
444 the CMAQ process analysis. A direct use of the process analysis output (in unit of ppbv hr⁻¹) can
445 be confusing as both **physiochemical** processes and underlying concentrations are inextricably
446 linked together. To be able to isolate each process (in unit of hr⁻¹), we normalize the outputs by
447 ozone concentrations. We average each process at the same hours used in calculating MDA8.
448 Figure 8 shows the major model processes, namely horizontal transport (horizontal advection plus
449 diffusion), vertical transport (vertical advection plus diffusion), dry deposition, and chemistry in
450 2020, 2019, and their differences. Positive (negative) values indicate a source (sink) for ozone.
451 Regarding the horizontal transport, the values mostly follow the transport pattern and are
452 dependent on whether the advected air mass is more or less polluted. The vertical transport
453 correlates with the PBLH which is an indicator of the atmospheric stability and turbulence,
454 although we should not rule out the impact of the subgrid convective transport that can occur
455 sporadically. Low PBLHs are usually associated with more stable (or sometimes capping
456 inversion) and weaker vertical mixing [e.g., Nevius and Evans, 2018]. Vertical transport which is
457 majorly dictated by the vertical diffusion is by far the most influential factor in the magnitude of

458 ozone [e.g., Cuchiara et al., 2014]. In contrast to NO_2 and HCHO , a stronger vertical diffusion
459 increases surface ozone due to positive gradients of ozone with respect to altitude. However, the
460 aerodynamic resistance controlling dry deposition velocity [Seinfeld and Pandis, 2006] is also a
461 function of turbulent transport. For example, during daytime, intensified turbulence exposes more
462 pollution to surface deposition. It is because of this reason that we see the dry deposition process
463 largely counteracting vertical transport. This will leave the chemistry process the major driver of
464 the ozone changes.

465 We separately sum the quantities of the physical processes and PO_3 contributing to MDA8
466 surface ozone changes binned to box L. The physical processes lead to -4.83 ppbv changes in the
467 MDA8 ozone mainly due to a relatively larger dry deposition in 2020, whereas $\text{P}(\text{O}_3)$ contributes
468 to $+5.89$ ppbv. The net effect is $+1.06$ ppbv which is slightly smaller than the simulated changes
469 in MDA8 ozone in this region ($+1.79$ ppbv). This apparent discrepancy is caused by the differences
470 in boundary and initial conditions which are not quantifiable by the process analysis and would
471 require additional sensitivity test. Nonetheless, we believe these numbers should provide
472 convincing evidence on the fact that chemistry has promoted the enhancements of surface ozone
473 during the lockdown.

474 Chemistry is also a function of meteorology, specifically solar radiation and temperature.
475 A typical scenario to isolate emissions from meteorology is by running the model with fixed
476 anthropogenic emissions (and boundary conditions) and subtracting the outputs from the variable
477 emission output. Figure 9 shows the contribution of anthropogenic emissions (VOCs and NO_x) to
478 the changes seen over the surface. The anthropogenic emissions make up roughly 58% of the
479 changes. The map is strongly in line with the changes in NO_x emissions constrained by TROPOMI.
480 The impact of meteorology plus biogenic changes (the former is dominant) highly correlates with
481 anomalies in both surface air temperature and photolysis rates **dictated by synoptic conditions**
482 **(Figure S17)**. We observe negligible ozone changes due to emissions over Iberian Peninsula
483 reinforcing the significance of the meteorological impacts [Ordóñez et al., 2020].

484 **3.4.Ozone chemistry**

485 Figure 10 shows the numerically-solved ozone production rates (PO_3) simulated by the
486 constrained model during the MDA8 hours period. We observe positive PO_3 in less polluted areas
487 and eastern Europe where biomass burning activities occurred in 2019 (see S1 and S2), while
488 negative PO_3 in major cities. Negative values in PO_3 are indicative of either loss in O_3 or $\text{O}_3\text{-NO}$

489 NO₂ partitioning. The difference in PO₃ between the two years suggests that the ozone
 490 enhancement in box L is caused by a reduction in negative PO₃ in 2020 over major cities compared
 491 to 2019. To examine which pathways are contributing to this pattern, we attempt to analytically
 492 reproduce the numerically-solved PO₃ (Figure 10) through two different equations: the first
 493 equation widely applied in photochemically active environments follows [Kleinman et al., 2002]:

$$\begin{aligned}
 P(O_3) = & k_{HO_2+NO}[HO_2][NO] + \sum k_{RO_{2i}+NO}[RO_{2i}][NO] \\
 & - k_{OH+NO_2+M}[OH][NO_2][M] - k_{HO_2+O_3}[HO_2][O_3] \\
 & - k_{OH+O_3}[OH][O_3] - k_{O(^1D)+H_2O}[O(^1D)][H_2O] - L(O_3) \\
 & + VOCs)
 \end{aligned} \tag{6}$$

494 This equation yields negative values only if the O₃ loss pathways including NO₂+OH, HO_x+O₃ ,
 495 O¹D+H₂O and O₃+VOCs dominate over the first two terms. The second equation which is
 496 independent of RO₂ and HO₂ concentrations [Thornton et al., 2002], is:

$$P(O_3) = jNO_2[NO_2] - k_{NO+O_3}[O_3][NO] \tag{7}$$

497 In summer, this equation tends to be positive during early afternoon, almost zero during afternoon
 498 (steady-state), and negative in early morning (or night) in which the second term (O₃ titration) is
 499 leading. Any abrupt changes in NO_x and VOC, and photolysis can directly affect Eq.7 moving PO₃
 500 out of the diel steady-state. The assumption of the steady-state (PO₃ from Eq.7 equals to zero) is
 501 also not valid if an air parcel is in the vicinity of high-emitting NO_x sources [Thornton et al., 2002].

502 Figure 11 displays the reactions rates of each individual component involved in Eq.6
 503 averaged during the MDA8 hours. HO₂+NO is the dominant chemical source of ozone correlating
 504 well with the changes in NO_x and prevailing chemical conditions regimes (NO_x-sensitive vs VOC-
 505 sensitive). Souri et al. [2020a] found the reaction of RO₂+NO to be primarily dependent on VOCs.
 506 Likewise, we observe a strong degree of correlation between the anomaly of RO₂+NO and that of
 507 VOCs (Figure S1 and S2). Figure 11 indicates that the chemical pathways of ozone loss are rather
 508 constant between the two years; therefore the largely negative PO₃ over urban areas shown
 509 previously in Figure 10 is not reproducible using this equation. Figure 12 shows the reactions rates
 510 of J_{NO₂}[NO₂], k_{NO+O₃}[NO][O₃], and the difference during the MDA8 hours. The difference maps
 511 replicate the largely negative PO₃ over cities suggesting that we are not in the diel steady-state,
 512 and O₃ titration is prevailing due to relatively low photochemistry in the springtime. Table 2 lists
 513 the averaged reactions rates involved in Eq.6 and 7 along with the numerically-solved PO₃ shown

514 in Figure 10 over box L. These numbers suggest that the major chemical pathways of enhanced
515 ozone are through $J_{\text{NO}_2}[\text{NO}_2]$ and $k_{\text{NO}+\text{O}_3}[\text{NO}][\text{O}_3]$, implying that $\text{O}_3\text{-NO-NO}_2$ partitioning is more
516 consequential than other chemical pathways. This analysis strongly coincides with Lee et al.
517 [2020] and Wyche et al. [2021] who observed roughly constant O_3+NO_2 concentrations over the
518 UK before and during the lockdown 2020.

519 **4. Summary**

520 The slowdown in human activities due to the COVID-19 pandemic had a large impact on
521 air pollution over Europe [Barré et al. 2020; Siccard et al., 2020; Sun et al., 2021]. Satellite
522 monitoring systems with large spatial coverage help shed light on the spatial and temporal extent
523 of those impacts. The relationships between satellite-derived columns and near-surface emissions
524 have proven difficult to fully establish without using realistic models, capable of providing insights
525 on the convoluted processes involving chemistry, dynamics, transport, and photochemistry and
526 therefore help with deciphering what anomaly maps of satellite concentrations are suggesting [e.g.,
527 Goldberg et al., 2020]. To address these challenges, we jointly constrained NO_x and VOC
528 emissions using TROPOMI HCHO and NO_2 columns following a non-linear Gauss Newton
529 method developed in Souri et al. [2020a], in addition to assimilating MODIS AOD observations
530 based on Jung et al. [2019]. The constrained emissions also permitted investigating the
531 simultaneous effects of **physiochemical** processes contributing to ozone formation, illuminating
532 the complexities associated with non-linear chemistry.

533 Several implications of the derived emissions for the months of March, April, and May
534 2020 (lockdown) relative to those in 2019 (baseline) were investigated. First, as previously
535 reported [Sicard et al., 2020; Barré et al. 2020], we observed a significant reduction in NO_x in
536 March (14-31%) in several major polluted regions including Paris, London, Madrid, and Milan.
537 The reductions were further seen in other cities such as Rome, Brussels, Frankfurt, Warsaw,
538 Belgrade, Kyiv, and Moscow (34-51%) in April. Second, NO_x emissions decreased drastically in
539 April rather than March in UK, Moscow, and Poland due to the timeline of restrictions. **Third, the**
540 **changes in NO_x suggested by TROPOMI NO_2 and the constrained model over northeastern**
541 **Germany in March and Eastern Europe in May were unrealistic, possibly due to observations or**
542 **the model issues. Fourth, we observed a weak observational constraint on VOC emissions from**
543 **TROPOMI HCHO except for lower latitudes.**

544 The constrained model calculations gave good representations of near-surface NO₂
545 changes in April (model: -21±17%, observation: -29±21%) in places where the top-down estimates
546 are strongly constrained by TROPOMI (averaging kernels > 0.5), but inferior representations in
547 other months, especially in May (model: -12±18%, observation: -25±20%). This tendency mainly
548 arose from TROPOMI observation frequencies; too few days (10-26% out of a month) in May due
549 to cloudiness precluded the determination of realistic NO_x emission changes.

550 We observed surface MDA8 ozone increase from both model and measurements in April
551 2020 with respect to the baseline. Comparisons of calculation by the constrained model in terms
552 of MDA8 surface ozone found a reasonable agreement with observations in the proximity of
553 central Europe in April (model: +3.73±3.94%, +1.79 ppbv, observation: +7.35±11.27%, +3.76
554 ppbv). These comparisons indicate that the performance of the constrained model to reproduce the
555 ozone enhancement feature is promising, suggesting fruitful information in TROPOMI, although
556 reasons behind the underestimation of the enhancement remained unexplained. It was clear that
557 the dominantly negative ozone production rates dictated by O₃-NO-NO₂ partitioning ($J_{\text{NO}_2}[\text{NO}_2]-$
558 $k_{\text{NO}+\text{O}_3}[\text{NO}][\text{O}_3]$) became less negative primarily due to the reduced NO_x emissions in urban areas
559 where O₃ titration occurred. This tendency was in agreement with studies of Lee et al. [2020] and
560 Wyche et al. [2021]. We found negligible differences in ozone production from $[\text{HO}_2+\text{RO}_2][\text{NO}]$
561 and ozone loss from O¹D+H₂O and O₃+HO_x between the two years suggesting photochemistry
562 was rather low in the springtime over Europe.

563 We further quantified the contributions of physical processes (transport, diffusion and dry
564 deposition) and chemistry to the formation/loss of ozone using the integrated process rates. The
565 physical processes decreased MDA8 ozone by -4.83 ppbv resulting from relatively larger dry
566 deposition in 2020, whereas chemistry (ozone production) augmented ozone levels by +5.89 ppbv,
567 indicating that rising ozone was primarily impacted by changes in chemistry. Enhanced air
568 temperature and photolysis in 2020, both of which were well captured in our model, also affected
569 chemistry. Experiments with fixed anthropogenic emissions underwent significant enhancement
570 in surface MDA8 ozone over central Europe, but those only contribute to 42% of the total
571 enhancement indicating that anthropogenic emissions were the major factor.

572 The results shown here reveal previously unquantified characteristics of ozone and its
573 precursors emission changes during the lockdown 2020 in Europe. We have been able to measure
574 the amount of changes along with the level of confidence in NO_x (and partly VOC emissions)

575 using a state-of-the-art inversion technique by leveraging satellite observations, which in turn,
576 allowed us to unravel the **physiochemical** processes contributing to increased ozone in Europe.
577 Unless a comprehensive air quality campaign targeting COVID-19 related lockdown is available,
578 we recommend that the impact of lockdown on air pollution should be examined through the lens
579 of well-established models constrained by publicly available data, especially those from space in
580 less cloudy environments.

581 **Author contributions**

582 AHS designed the research, analyzed the data, conducted the inverse modeling and atmospheric
583 modeling (for CMAQ, GEOS-Chem, WRF, and MEGAN), made all figures, and wrote the paper.
584 JB validated WRF-CMAQ model and reformatted the surface observation files. CRN and GGA
585 did literature review regarding the TROPOMI validation. YJ validated MODIS AOD. DW helped
586 with implementing the AOD assimilation framework. KC, JM, and XL guided the discussion. All
587 authors contributed to discussion and edited the paper.

588 **Data availability**

589 The atmospheric inversion data are publicly available from Souri et al. [2021]. The model outputs
590 are available upon the request from ahsouri@cfa.harvard.edu. The links on where to download
591 surface and satellite observations that are used in this study are already provided in the text.

592 **Acknowledgments**

593 Amir H. Souri acknowledges supports from the Smithsonian Astrophysical Observatory (SAO)
594 Scholarly Award (40488100AA50203), MethaneSAT LLC, and Environmental Defense Fund. J.
595 Bak acknowledges Basic Science Research Program through the National Research Foundation of
596 Korea (NRF) funded by the Ministry of Education (2020R1A6A1A03044834). Both calculations
597 and simulations are done on the Smithsonian Institution High-Performance Cluster (SI/HPC)
598 (<https://doi.org/10.25572/SIHPC>). The views expressed in this manuscript are those of the authors
599 alone and do not necessarily reflect the views and policies of the U.S. Environmental Protection
600 Agency. EPA does not endorse any products or commercial services mentioned in this publication.
601

602

603 **References**

- 604 Auligné, T., McNally, A. P., and Dee, D. P.: Adaptive bias correction for satellite data in a
605 numerical weather prediction system, *Quarterly Journal of the Royal Meteorological*
606 *Society*, 133, 631–642, <https://doi.org/10.1002/qj.56>, 2007.
- 607 Barré, J., Petetin, H., Colette, A., Guevara, M., Peuch, V.-H., Rouil, L., Engelen, R., Inness, A.,
608 Flemming, J., Pérez García-Pando, C., Bowdalo, D., Meleux, F., Geels, C., Christensen,
609 J. H., Gauss, M., Benedictow, A., Tsyro, S., Friese, E., Struzewska, J., Kaminski, J. W.,
610 Douros, J., Timmermans, R., Robertson, L., Adani, M., Jorba, O., Joly, M. and
611 Kouznetsov, R.: Estimating lockdown induced European NO₂ changes, *Atmospheric*
612 *Chemistry and Physics Discussions*, 1–28, <https://doi.org/10.5194/acp-2020-995>, 2020.
- 613 Baudic, A., Gros, V., Sauvage, S., Locoge, N., Sanchez, O., Sarda-Estève, R., Kalogridis, C.,
614 Petit, J.-E., Bonnaire, N., Baisnée, D., Favez, O., Albinet, A., Sciare, J. and Bonsang, B.:
615 Seasonal variability and source apportionment of volatile organic compounds (VOCs) in
616 the Paris megacity (France), *Atmospheric Chemistry and Physics*, 16(18), 11961–11989,
617 <https://doi.org/10.5194/acp-16-11961-2016>, 2016.
- 618 Bekbulat, B., Apte, J. S., Millet, D. B., Robinson, A. L., Wells, K. C., Presto, A. A., and
619 Marshall, J. D.: Changes in criteria air pollution levels in the US before, during, and after
620 Covid-19 stay-at-home orders: Evidence from regulatory monitors, *Science of The Total*
621 *Environment*, 769, 144693, <https://doi.org/10.1016/j.scitotenv.2020.144693>, 2021.
- 622 Bertram, T. H. and Thornton, J. A.: Toward a general parameterization of N₂O₅ reactivity on
623 aqueous particles: the competing effects of particle liquid water, nitrate and chloride, 9,
624 8351–8363, <https://doi.org/10.5194/acp-9-8351-2009>, 2009.
- 625 Boersma, K. F., Eskes, H. J., Richter, A., De Smedt, I., Lorente, A., Beirle, S., van Geffen, J. H.
626 G. M., Zara, M., Peters, E., Van Roozendaal, M., Wagner, T., Maasakkers, J. D., van der
627 A, R. J., Nightingale, J., De Rudder, A., Irie, H., Pinardi, G., Lambert, J.-C. and
628 Compernelle, S. C.: Improving algorithms and uncertainty estimates for satellite NO₂
629 retrievals: results from the quality assurance for the essential climate variables
630 (QA4ECV) project, *Atmospheric Measurement Techniques*, 11(12), 6651–6678,
631 <https://doi.org/10.5194/amt-11-6651-2018>, 2018.
- 632 Castellanos, P. and Boersma, K. F.: Reductions in nitrogen oxides over Europe driven by
633 environmental policy and economic recession, *Scientific Reports*, 2(1), 265,
634 <https://doi.org/10.1038/srep00265>, 2012.
- 635 Chan, K. L., Wiegner, M., van Geffen, J., De Smedt, I., Alberti, C., Cheng, Z., Ye, S. and Wenig,
636 M.: MAX-DOAS measurements of tropospheric NO₂ and HCHO in Munich and the
637 comparison to OMI and TROPOMI satellite observations, *Atmospheric Measurement*
638 *Techniques*, 13(8), 4499–4520, <https://doi.org/10.5194/amt-13-4499-2020>, 2020.
- 639 Cooper, M. J., Martin, R. V., Hammer, M. S., and McLinden, C. A.: An Observation-Based
640 Correction for Aerosol Effects on Nitrogen Dioxide Column Retrievals Using the
641 Absorbing Aerosol Index, 46, 8442–8452, <https://doi.org/10.1029/2019GL083673>, 2019.
- 642 Copernicus Sentinel data processed by ESA, Koninklijk Nederlands Meteorologisch Instituut
643 (KNMI) (2019), Sentinel-5P TROPOMI Tropospheric NO₂ 1-Orbit L2 5.5km x 3.5km,
644 Greenbelt, MD, USA, Goddard Earth Sciences Data and Information Services Center
645 (GES DISC), Accessed: [Data Access Date], <https://doi.org/10.5270/S5P-s4ljg54>

646 Cuchiara, G. C., Li, X., Carvalho, J. and Rappenglück, B.: Intercomparison of planetary
647 boundary layer parameterization and its impacts on surface ozone concentration in the
648 WRF/Chem model for a case study in Houston/Texas, *Atmospheric Environment*, 96,
649 175–185, <https://doi.org/10.1016/j.atmosenv.2014.07.013>, 2014.

650 Dickerson, R. R., Anderson, D. C. and Ren, X.: On the use of data from commercial NOx
651 analyzers for air pollution studies, *Atmospheric Environment*, 214, 116873,
652 <https://doi.org/10.1016/j.atmosenv.2019.116873>, 2019.

653 Emanuel, K. A.: *Atmospheric Convection*, 1st edition., Oxford University Press, New York.,
654 1994.

655 Fauci, A. S., Lane, H. C. and Redfield, R. R.: Covid-19 — Navigating the Uncharted, *New
656 England Journal of Medicine*, 382(13), 1268–1269,
657 <https://doi.org/10.1056/NEJMe2002387>, 2020.

658 Gaubert, B., Bouarar, I., Doumbia, T., Liu, Y., Stavrakou, T., Deroubaix, A., Darras, S.,
659 Elguindi, N., Granier, C., Lacey, F., Müller, J.-F., Shi, X., Tilmes, S., Wang, T., and
660 Brasseur, G. P.: Global Changes in Secondary Atmospheric Pollutants During the 2020
661 COVID-19 Pandemic, 126, e2020JD034213, <https://doi.org/10.1029/2020JD034213>,
662 2021.

663 Goldberg, D. L., Anenberg, S. C., Griffin, D., McLinden, C. A., Lu, Z. and Streets, D. G.:
664 Disentangling the Impact of the COVID-19 Lockdowns on Urban NO₂ From Natural
665 Variability, *Geophysical Research Letters*, 47(17), e2020GL089269,
666 <https://doi.org/10.1029/2020GL089269>, 2020.

667 Grange, S. K., Farren, N. J., Vaughan, A. R., Rose, R. A. and Carslaw, D. C.: Strong
668 Temperature Dependence for Light-Duty Diesel Vehicle NO_x Emissions, *Environ. Sci.
669 Technol.*, 53(11), 6587–6596, <https://doi.org/10.1021/acs.est.9b01024>, 2019.

670 Grell, G. A. and Dévényi, D.: A generalized approach to parameterizing convection combining
671 ensemble and data assimilation techniques, *Geophysical Research Letters*, 29(14), 38-1-
672 38–4, <https://doi.org/10.1029/2002GL015311>, 2002.

673 Griffin, D., Zhao, X., McLinden, C. A., Boersma, F., Bourassa, A., Dammers, E., Degenstein,
674 D., Eskes, H., Fehr, L., Fioletov, V., Hayden, K., Kharol, S. K., Li, S.-M., Makar, P.,
675 Martin, R. V., Mihele, C., Mittermeier, R. L., Krotkov, N., Snee, M., Lamsal, L. N.,
676 Linden, M. ter, Geffen, J. van, Veefkind, P. and Wolde, M.: High-Resolution Mapping of
677 Nitrogen Dioxide With TROPOMI: First Results and Validation Over the Canadian Oil
678 Sands, *Geophysical Research Letters*, 46(2), 1049–1060,
679 <https://doi.org/10.1029/2018GL081095>, 2019.

680 Guenther, A. B., Jiang, X., Heald, C. L., Sakulyanontvittaya, T., Duhl, T., Emmons, L. K. and
681 Wang, X.: The Model of Emissions of Gases and Aerosols from Nature version 2.1
682 (MEGAN2.1): an extended and updated framework for modeling biogenic emissions,
683 *Geoscientific Model Development*, 5(6), 1471–1492, [https://doi.org/10.5194/gmd-5-
684 1471-2012](https://doi.org/10.5194/gmd-5-1471-2012), 2012.

685 He, G., Pan, Y. and Tanaka, T.: The short-term impacts of COVID-19 lockdown on urban air
686 pollution in China, *Nature Sustainability*, 3(12), 1005–1011,
687 <https://doi.org/10.1038/s41893-020-0581-y>, 2020.

688 Hoesly, R. M., Smith, S. J., Feng, L., Klimont, Z., Janssens-Maenhout, G., Pitkanen, T., Seibert,
689 J. J., Vu, L., Andres, R. J., Bolt, R. M., Bond, T. C., Dawidowski, L., Kholod, N.,
690 Kurokawa, J., Li, M., Liu, L., Lu, Z., Moura, M. C. P., O'Rourke, P. R. and Zhang, Q.:
691 Historical (1750–2014) anthropogenic emissions of reactive gases and aerosols from the

692 Community Emissions Data System (CEDS), *Geoscientific Model Development*, 11(1),
693 369–408, <https://doi.org/10.5194/gmd-11-369-2018>, 2018.

694 Huang, M., Crawford, J. H., DiGangi, J. P., Carmichael, G. R., Bowman, K. W., Kumar, S. V.,
695 and Zhan, X.: Satellite soil moisture data assimilation impacts on modeling weather
696 variables and ozone in the southeastern US – Part 1: An overview, 21, 11013–11040,
697 <https://doi.org/10.5194/acp-21-11013-2021>, 2021.

698 Jacob, D. J.: Heterogeneous chemistry and tropospheric ozone, *Atmospheric Environment*,
699 34(12), 2131–2159, [https://doi.org/10.1016/S1352-2310\(99\)00462-8](https://doi.org/10.1016/S1352-2310(99)00462-8), 2000.

700 Jacobson, M. Z.: *Fundamentals of Atmospheric Modeling*, 2nd ed., Cambridge University Press,
701 Cambridge., 2005.

702 Janjić, T., Bormann, N., Bocquet, M., Carton, J. A., Cohn, S. E., Dance, S. L., Losa, S. N.,
703 Nichols, N. K., Potthast, R., Waller, J. A. and Weston, P.: On the representation error in
704 data assimilation, *Quarterly Journal of the Royal Meteorological Society*, 144(713),
705 1257–1278, <https://doi.org/10.1002/qj.3130>, 2018.

706 Judd, L. M., Al-Saadi, J. A., Szykman, J. J., Valin, L. C., Janz, S. J., Kowalewski, M. G., Eskes,
707 H. J., Veeffkind, J. P., Cede, A., Mueller, M., Gebetsberger, M., Swap, R., Pierce, R. B.,
708 Nowlan, C. R., Abad, G. G., Nehrir, A. and Williams, D.: Evaluating Sentinel-5P
709 TROPOMI tropospheric NO₂ column densities with airborne and Pandora spectrometers
710 near New York City and Long Island Sound, *Atmospheric Measurement Techniques*,
711 13(11), 6113–6140, <https://doi.org/10.5194/amt-13-6113-2020>, 2020.

712 Jung, J., Souri, A. H., Wong, D. C., Lee, S., Jeon, W., Kim, J. and Choi, Y.: The Impact of the
713 Direct Effect of Aerosols on Meteorology and Air Quality Using Aerosol Optical Depth
714 Assimilation During the KORUS-AQ Campaign, *Journal of Geophysical Research:*
715 *Atmospheres*, 124(14), 8303–8319, <https://doi.org/10.1029/2019JD030641>, 2019.

716 Jung, Y., González Abad, G., Nowlan, C. R., Chance, K., Liu, X., Torres, O., and Ahn, C.:
717 Explicit Aerosol Correction of OMI Formaldehyde Retrievals, *Earth and Space Science*,
718 6, 2087–2105, <https://doi.org/10.1029/2019EA000702>, 2019.

719 Ke, Y., Leung, L. R., Huang, M., Coleman, A. M., Li, H. and Wigmosta, M. S.: Development of
720 high resolution land surface parameters for the Community Land Model, *Geoscientific*
721 *Model Development*, 5(6), 1341–1362, <https://doi.org/10.5194/gmd-5-1341-2012>, 2012.

722 Kleinman, L. I., Daum, P. H., Lee, Y.-N., Nunnermacker, L. J., Springston, S. R., Weinstein-
723 Lloyd, J. and Rudolph, J.: Ozone production efficiency in an urban area, *Journal of*
724 *Geophysical Research: Atmospheres*, 107(D23), ACH 23-1-ACH 23-12,
725 <https://doi.org/10.1029/2002JD002529>, 2002.

726 Krotkov, N. A., McLinden, C. A., Li, C., Lamsal, L. N., Celarier, E. A., Marchenko, S. V.,
727 Swartz, W. H., Bucsela, E. J., Joiner, J., Duncan, B. N., Boersma, K. F., Veeffkind, J. P.,
728 Levelt, P. F., Fioletov, V. E., Dickerson, R. R., He, H., Lu, Z. and Streets, D. G.: Aura
729 OMI observations of regional SO₂ and NO₂ pollution changes from 2005 to 2015,
730 *Atmospheric Chemistry and Physics*, 16(7), 4605–4629, [https://doi.org/10.5194/acp-16-](https://doi.org/10.5194/acp-16-4605-2016)
731 [4605-2016](https://doi.org/10.5194/acp-16-4605-2016), 2016.

732 Lamsal, L. N., Martin, R. V., Donkelaar, A. van, Steinbacher, M., Celarier, E. A., Bucsela, E.,
733 Dunlea, E. J. and Pinto, J. P.: Ground-level nitrogen dioxide concentrations inferred from
734 the satellite-borne Ozone Monitoring Instrument, *Journal of Geophysical Research:*
735 *Atmospheres*, 113(D16), <https://doi.org/10.1029/2007JD009235>, 2008.

736 Le Quéré, C., Jackson, R. B., Jones, M. W., Smith, A. J. P., Abernethy, S., Andrew, R. M., De-
737 Gol, A. J., Willis, D. R., Shan, Y., Canadell, J. G., Friedlingstein, P., Creutzig, F. and

738 Peters, G. P.: Temporary reduction in daily global CO₂ emissions during the COVID-19
739 forced confinement, *Nature Climate Change*, 10(7), 647–653,
740 <https://doi.org/10.1038/s41558-020-0797-x>, 2020.

741 Le, T., Wang, Y., Liu, L., Yang, J., Yung, Y. L., Li, G. and Seinfeld, J. H.: Unexpected air
742 pollution with marked emission reductions during the COVID-19 outbreak in China,
743 *Science*, 369(6504), 702–706, <https://doi.org/10.1126/science.abb7431>, 2020.

744 Lee, J. D., Drysdale, W. S., Finch, D. P., Wilde, S. E. and Palmer, P. I.: UK surface NO₂ levels
745 dropped by 42% during the COVID-19 lockdown: impact on surface O₃,
746 *Atmospheric Chemistry and Physics*, 20(24), 15743–15759, <https://doi.org/10.5194/acp-20-15743-2020>, 2020.

748 Lelieveld, J., Berresheim, H., Borrmann, S., Crutzen, P. J., Dentener, F. J., Fischer, H., Feichter,
749 J., Flatau, P. J., Heland, J., Holzinger, R., Kormann, R., Lawrence, M. G., Levin, Z.,
750 Markowicz, K. M., Mihalopoulos, N., Minikin, A., Ramanathan, V., Reus, M. de,
751 Roelofs, G. J., Scheeren, H. A., Sciare, J., Schlager, H., Schultz, M., Siegmund, P., Steil,
752 B., Stephanou, E. G., Stier, P., Traub, M., Warneke, C., Williams, J., and Ziereis, H.:
753 Global Air Pollution Crossroads over the Mediterranean, 298, 794–799,
754 <https://doi.org/10.1126/science.1075457>, 2002.

755 Levy, R. C., Mattoo, S., Munchak, L. A., Remer, L. A., Sayer, A. M., Patadia, F. and Hsu, N. C.:
756 The Collection 6 MODIS aerosol products over land and ocean, *Atmospheric*
757 *Measurement Techniques*, 6(11), 2989–3034, <https://doi.org/10.5194/amt-6-2989-2013>,
758 2013.

759 Li, K. and Lin, B.: Impacts of urbanization and industrialization on energy consumption/CO₂
760 emissions: Does the level of development matter?, *Renewable and Sustainable Energy*
761 *Reviews*, 52, 1107–1122, <https://doi.org/10.1016/j.rser.2015.07.185>, 2015.

762 Lin, Y.-L., Farley, R. D. and Orville, H. D.: Bulk Parameterization of the Snow Field in a Cloud
763 Model, *Journal of Applied Meteorology and Climatology*, 22(6), 1065–1092,
764 [https://doi.org/10.1175/1520-0450\(1983\)022<1065:BPOTSF>2.0.CO;2](https://doi.org/10.1175/1520-0450(1983)022<1065:BPOTSF>2.0.CO;2), 1983.

765 Liu, F., Page, A., Strode, S. A., Yoshida, Y., Choi, S., Zheng, B., Lamsal, L. N., Li, C., Krotkov,
766 N. A., Eskes, H., A. R. van der, Veeffkind, P., Levelt, P. F., Hauser, O. P. and Joiner, J.:
767 Abrupt decline in tropospheric nitrogen dioxide over China after the outbreak of COVID-
768 19, *Science Advances*, 6(28), eabc2992, <https://doi.org/10.1126/sciadv.abc2992>, 2020.

769 Lorenz, E. N.: Deterministic Nonperiodic Flow, *Journal of the Atmospheric Sciences*, 20(2),
770 130–141, [https://doi.org/10.1175/1520-0469\(1963\)020<0130:DNF>2.0.CO;2](https://doi.org/10.1175/1520-0469(1963)020<0130:DNF>2.0.CO;2), 1963.

771 Marais, E. A., Jacob, D. J., Kurosu, T. P., Chance, K., Murphy, J. G., Reeves, C., Mills, G.,
772 Casadio, S., Millet, D. B., Barkley, M. P., Paulot, F. and Mao, J.: Isoprene emissions in
773 Africa inferred from OMI observations of formaldehyde columns, *Atmospheric*
774 *Chemistry and Physics*, 12(14), 6219–6235, <https://doi.org/10.5194/acp-12-6219-2012>,
775 2012.

776 Martin, R. V., Chance, K., Jacob, D. J., Kurosu, T. P., Spurr, R. J. D., Bucsele, E., Gleason, J. F.,
777 Palmer, P. I., Bey, I., Fiore, A. M., Li, Q., Yantosca, R. M., and Koelemeijer, R. B. A.:
778 An improved retrieval of tropospheric nitrogen dioxide from GOME, 107, ACH 9-1-
779 ACH 9-21, <https://doi.org/10.1029/2001JD001027>, 2002.

780 Miyazaki, K., Bowman, K., Sekiya, T., Jiang, Z., Chen, X., Eskes, H., Ru, M., Zhang, Y. and
781 Shindell, D.: Air Quality Response in China Linked to the 2019 Novel Coronavirus
782 (COVID-19) Lockdown, *Geophysical Research Letters*, 47(19), e2020GL089252,
783 <https://doi.org/10.1029/2020GL089252>, 2020.

784 Nevius, D. S. and Evans, C.: The Influence of Vertical Advection Discretization in the WRF-
785 ARW Model on Capping Inversion Representation in Warm-Season, Thunderstorm-
786 Supporting Environments, *Weather and Forecasting*, 33(6), 1639–1660,
787 <https://doi.org/10.1175/WAF-D-18-0103.1>, 2018.

788 Okruszek, Ł., Aniszewska-Stańczuk, A., Piejka, A., Wiśniewska, M., and Żurek, K.: Safe but
789 Lonely? Loneliness, Anxiety, and Depression Symptoms and COVID-19, *Front.*
790 *Psychol.*, 11, <https://doi.org/10.3389/fpsyg.2020.579181>, 2020.

791 Ordóñez, C., Garrido-Perez, J. M. and García-Herrera, R.: Early spring near-surface ozone in
792 Europe during the COVID-19 shutdown: Meteorological effects outweigh emission
793 changes, *Science of The Total Environment*, 747, 141322,
794 <https://doi.org/10.1016/j.scitotenv.2020.141322>, 2020.

795 Parrish, D. D., Lamarque, J.-F., Naik, V., Horowitz, L., Shindell, D. T., Staehelin, J., Derwent,
796 R., Cooper, O. R., Tanimoto, H., Volz-Thomas, A., Gilge, S., Scheel, H.-E., Steinbacher,
797 M. and Fröhlich, M.: Long-term changes in lower tropospheric baseline ozone
798 concentrations: Comparing chemistry-climate models and observations at northern
799 midlatitudes, *Journal of Geophysical Research: Atmospheres*, 119(9), 5719–5736,
800 <https://doi.org/10.1002/2013JD021435>, 2014.

801 Pleim, J. E.: A Combined Local and Nonlocal Closure Model for the Atmospheric Boundary
802 Layer. Part I: Model Description and Testing, *Journal of Applied Meteorology and*
803 *Climatology*, 46(9), 1383–1395, <https://doi.org/10.1175/JAM2539.1>, 2007.

804 Pouyaei, A., Sadeghi, B., Choi, Y., Jung, J., Souri, A. H., Zhao, C., and Song, C. H.:
805 Development and Implementation of a Physics-Based Convective Mixing Scheme in the
806 Community Multiscale Air Quality Modeling Framework, 13, e2021MS002475,
807 <https://doi.org/10.1029/2021MS002475>, 2021.

808 Rodgers, C. D.: *Inverse Methods for Atmospheric Sounding: Theory and Practice*, WORLD
809 SCIENTIFIC, Oxford, 2000.

810 Rappenglück, B., Ackermann, L., Alvarez, S., Golovko, J., Buhr, M., Field, R. A., Soltis, J.,
811 Montague, D. C., Hauze, B., Adamson, S., Risch, D., Wilkerson, G., Bush, D.,
812 Stoeckenius, T., and Keslar, C.: Strong wintertime ozone events in the Upper Green
813 River basin, Wyoming, 14, 4909–4934, <https://doi.org/10.5194/acp-14-4909-2014>, 2014.

814 Salma, I., Vörösmarty, M., Gyöngyösi, A. Z., Thén, W. and Weidinger, T.: What can we learn
815 about urban air quality with regard to the first outbreak of the COVID-19 pandemic? A
816 case study from central Europe, *Atmospheric Chemistry and Physics*, 20(24), 15725–
817 15742, <https://doi.org/10.5194/acp-20-15725-2020>, 2020.

818 Seinfeld, J. H. and Pandis, S. N.: *Atmospheric Chemistry and Physics: From Air Pollution to*
819 *Climate Change*, 2nd edition., Wiley-Interscience, Hoboken, N.J., 2006.

820 Shi, X. and Brasseur, G. P.: The Response in Air Quality to the Reduction of Chinese Economic
821 Activities During the COVID-19 Outbreak, *Geophysical Research Letters*, 47(11),
822 e2020GL088070, <https://doi.org/10.1029/2020GL088070>, 2020.

823 Sicard, P., De Marco, A., Agathokleous, E., Feng, Z., Xu, X., Paoletti, E., Rodriguez, J. J. D. and
824 Calatayud, V.: Amplified ozone pollution in cities during the COVID-19 lockdown,
825 *Science of The Total Environment*, 735, 139542,
826 <https://doi.org/10.1016/j.scitotenv.2020.139542>, 2020.

827 Sillman, S.: The relation between ozone, NO_x and hydrocarbons in urban and polluted rural
828 environments, *Atmospheric Environment*, 33(12), 1821–1845,
829 [https://doi.org/10.1016/S1352-2310\(98\)00345-8](https://doi.org/10.1016/S1352-2310(98)00345-8), 1999.

830 Silvern, R. F., Jacob, D. J., Mickley, L. J., Sulprizio, M. P., Travis, K. R., Marais, E. A., Cohen,
831 R. C., Laughner, J. L., Choi, S., Joiner, J. and Lamsal, L. N.: Using satellite observations
832 of tropospheric NO₂ columns to infer long-term trends in US NO_x emissions: the
833 importance of accounting for the free tropospheric NO₂ background, *Atmospheric
834 Chemistry and Physics*, 19(13), 8863–8878, <https://doi.org/10.5194/acp-19-8863-2019>,
835 2019.

836 Skamarock, W. C. and Klemp, J. B.: A time-split nonhydrostatic atmospheric model for weather
837 research and forecasting applications, *Journal of Computational Physics*, 227(7), 3465–
838 3485, <https://doi.org/10.1016/j.jcp.2007.01.037>, 2008.

839 Souri, A. H., Nowlan, C. R., González Abad, G., Zhu, L., Blake, D. R., Fried, A., Weinheimer,
840 A. J., Wisthaler, A., Woo, J.-H., Zhang, Q., Chan Miller, C. E., Liu, X. and Chance, K.:
841 An inversion of NO_x and non-methane volatile organic compound (NMVOC) emissions
842 using satellite observations during the KORUS-AQ campaign and implications for
843 surface ozone over East Asia, *Atmospheric Chemistry and Physics*, 20(16), 9837–9854,
844 <https://doi.org/10.5194/acp-20-9837-2020>, 2020a.

845 Souri, A. H., Nowlan, C. R., Wolfe, G. M., Lamsal, L. N., Chan Miller, C. E., Abad, G. G., Janz,
846 S. J., Fried, A., Blake, D. R., Weinheimer, A. J., Diskin, G. S., Liu, X. and Chance, K.:
847 Revisiting the effectiveness of HCHO/NO₂ ratios for inferring ozone sensitivity to its
848 precursors using high resolution airborne remote sensing observations in a high ozone
849 episode during the KORUS-AQ campaign, *Atmospheric Environment*, 224, 117341,
850 <https://doi.org/10.1016/j.atmosenv.2020.117341>, 2020b.

851 Souri, A. H., Choi, Y., Jeon, W., Kochanski, A. K., Diao, L., Mandel, J., Bhawe, P. V., and Pan,
852 S.: Quantifying the Impact of Biomass Burning Emissions on Major Inorganic Aerosols
853 and Their Precursors in the U.S., 122, 12,020-12,041,
854 <https://doi.org/10.1002/2017JD026788>, 2017.

855 Souri, Amir H., Chance, K., Bak, J., Nowlan, C., González Abad, G., Jung, Y., Wong, D., Mao,
856 J., Liu, X.: COVID-19-Europe-Ozone-NO_x-VOC, Mendeley Data, V1, doi:
857 10.17632/jchfxsrvsb.1, 2021

858 Souri, Amir H., Chance, K., Sun, K., Liu, X., Johnson, M.S., Dealing with Spatial Heterogeneity
859 in Pointwise to Areal Data Comparisons, Submitted to *Atmospheric Measurement
860 Techniques*, 2021

861 Stavrou, T., Müller, J.-F., Bauwens, M., De Smedt, I., Van Roozendaal, M., Guenther, A.,
862 Wild, M. and Xia, X.: Isoprene emissions over Asia 1979–2012: impact of climate
863 and land-use changes, *Atmospheric Chemistry and Physics*, 14(9), 4587–4605,
864 <https://doi.org/10.5194/acp-14-4587-2014>, 2014.

865 Su, T., Li, Z. and Kahn, R.: Relationships between the planetary boundary layer height and
866 surface pollutants derived from lidar observations over China: regional pattern and
867 influencing factors, *Atmospheric Chemistry and Physics*, 18(21), 15921–15935,
868 <https://doi.org/10.5194/acp-18-15921-2018>, 2018.

869 Sun, K., Li, L., Jagini, S., and Li, D.: A Satellite Data-Driven Framework to Rapidly Quantify
870 Air Basin-Scale NO_x Emission and Its Application to the Po Valley during
871 the COVID-19 Pandemic, 1–29, <https://doi.org/10.5194/acp-2021-268>, 2021.

872 Thornton, J. A., Wooldridge, P. J., Cohen, R. C., Martinez, M., Harder, H., Brune, W. H.,
873 Williams, E. J., Roberts, J. M., Fehsenfeld, F. C., Hall, S. R., Shetter, R. E., Wert, B. P.
874 and Fried, A.: Ozone production rates as a function of NO_x abundances and HO_x
875 production rates in the Nashville urban plume, *Journal of Geophysical Research*:

876 Atmospheres, 107(D12), ACH 7-1-ACH 7-17, <https://doi.org/10.1029/2001JD000932>,
877 2002.

878 United Nations Conference on Trade and Development Report, Accessed Dec 2020,
879 https://unctad.org/system/files/official-document/dtltlbinf2020d1_en.pdf

880 Valin, L. C., Fiore, A. M., Chance, K. and Abad, G. G.: The role of OH production in
881 interpreting the variability of CH₂O columns in the southeast U.S., *Journal of*
882 *Geophysical Research: Atmospheres*, 121(1), 478–493,
883 <https://doi.org/10.1002/2015JD024012>, 2016.

884 Verhoelst, T., Compornolle, S., Pinardi, G., Lambert, J.-C., Eskes, H. J., Eichmann, K.-U.,
885 Fjæraa, A. M., Granville, J., Niemeijer, S., Cede, A., Tiefengraber, M., Hendrick, F.,
886 Pazmiño, A., Bais, A., Bazureau, A., Boersma, K. F., Bognar, K., Dehn, A., Donner, S.,
887 Elokhov, A., Gebetsberger, M., Goutail, F., Grutter de la Mora, M., Gruzdev, A., Gratsea,
888 M., Hansen, G. H., Irie, H., Jepsen, N., Kanaya, Y., Karagiozidis, D., Kivi, R., Kreher,
889 K., Levelt, P. F., Liu, C., Müller, M., Navarro Comas, M., Peters, A. J. M., Pommereau,
890 J.-P., Portafaix, T., Prados-Roman, C., Puentedura, O., Querel, R., Remmers, J., Richter,
891 A., Rimmer, J., Rivera Cárdenas, C., Saavedra de Miguel, L., Sinyakov, V. P., Stremme,
892 W., Strong, K., Van Roozendaal, M., Veeckind, J. P., Wagner, T., Wittrock, F., Yela
893 González, M. and Zehner, C.: Ground-based validation of the Copernicus Sentinel-5P
894 TROPOMI NO₂ measurements with the NDACC ZSL-DOAS, MAX-DOAS and
895 Pandonia global networks, *Atmospheric Measurement Techniques*, 14(1), 481–510,
896 <https://doi.org/10.5194/amt-14-481-2021>, 2021.

897 Wang, P., PETERS, A., van Geffen, J., Tuinder, O., Stammes, P. and Kinne, S.: Shipborne MAX-
898 DOAS measurements for validation of TROPOMI NO₂ products, *Atmospheric*
899 *Measurement Techniques*, 13(3), 1413–1426, <https://doi.org/10.5194/amt-13-1413-2020>,
900 2020.

901 Wang, W., Parrish, D. D., Li, X., Shao, M., Liu, Y., Mo, Z., Lu, S., Hu, M., Fang, X., Wu, Y.,
902 Zeng, L. and Zhang, Y.: Exploring the drivers of the increased ozone production in
903 Beijing in summertime during 2005–2016, *Atmospheric Chemistry and Physics*, 20(24),
904 15617–15633, <https://doi.org/10.5194/acp-20-15617-2020>, 2020.

905 Wolfe, G. M., Kaiser, J., Hanisco, T. F., Keutsch, F. N., de Gouw, J. A., Gilman, J. B., Graus,
906 M., Hatch, C. D., Holloway, J., Horowitz, L. W., Lee, B. H., Lerner, B. M., Lopez-
907 Hilifiker, F., Mao, J., Marvin, M. R., Peischl, J., Pollack, I. B., Roberts, J. M., Ryerson,
908 T. B., Thornton, J. A., Veres, P. R. and Warneke, C.: Formaldehyde production from
909 isoprene oxidation across NO_x regimes, *Atmospheric Chemistry and Physics*, 16(4),
910 2597–2610, <https://doi.org/10.5194/acp-16-2597-2016>, 2016.

911 Wyche, K. P., Nichols, M., Parfitt, H., Beckett, P., Gregg, D. J., Smallbone, K. L. and Monks, P.
912 S.: Changes in ambient air quality and atmospheric composition and reactivity in the
913 South East of the UK as a result of the COVID-19 lockdown, *Science of The Total*
914 *Environment*, 755, 142526, <https://doi.org/10.1016/j.scitotenv.2020.142526>, 2021.

915 Xiu, A. and Pleim, J. E.: Development of a Land Surface Model. Part I: Application in a
916 Mesoscale Meteorological Model, *Journal of Applied Meteorology and Climatology*,
917 40(2), 192–209, [https://doi.org/10.1175/1520-0450\(2001\)040<0192:DOALSM>2.0.CO;2](https://doi.org/10.1175/1520-0450(2001)040<0192:DOALSM>2.0.CO;2), 2001.

919 Yienger, J. J. and Levy, H.: Empirical model of global soil-biogenic NO_x emissions, *Journal of*
920 *Geophysical Research*, 100(D6), 11447–11464, <https://doi.org/10.1029/95JD00370>,
921 1995.

922 Zhao, X., Griffin, D., Fioletov, V., McLinden, C., Cede, A., Tiefengraber, M., Müller, M.,
923 Bogner, K., Strong, K., Boersma, F., Eskes, H., Davies, J., Ogyu, A. and Lee, S. C.:
924 Assessment of the quality of TROPOMI high-spatial-resolution NO₂ data products in the
925 Greater Toronto Area, Atmospheric Measurement Techniques, 13(4), 2131–2159,
926 <https://doi.org/10.5194/amt-13-2131-2020>, 2020.

927

928

929

930

931

932

933

934

935

936
 937
 938
 939
 940

Table 1. Statistics reported in several validations studies comparing TROPOMI tropospheric NO₂ against independent observations.

Study	Location	Time Period	Benchmark Instrument	Bias (low)	Dispersion	Modification	Modified Bias (low)
Chan et al. 2020	Munich	May 2018-Apr 2019	MAX-DOAS	30%	N/A	In-situ MAX-DOAS profiles	17%
Griffin et al. 2019	Canadian Oil Sands	Mar-May 2018 (v1.01)	Pandora (direct Sun)	15-30%	N/A	Higher resolution profiles (10 km) and albedo	0-25%
Judd et al. 2020	New York	Jun-Sep 2018	GeoTASO	19-33%	N/A	Higher resolution profiles (12 km)	7-19%
Verhoelst et al. 2020	Global	Apr 2018-Feb 2020	MAX-DOAS	37% (average), 23-51% (range)	3.5×10^{15} molec/cm ²	N/A	N/A
Wang P. et al. 2020	Atlantic and Pacific Oceans	4 campaigns during Dec 2018-Jul 2019	MAX-DOAS	Negligible	N/A	N/A	N/A
Zhao et al. 2020	Greater Toronto Area	Mar 2018-Mar 2019	Pandora (direct Sun)	24-28% (suburban/urban) +4-10% (rural)		Higher resolution profiles (10 km) and albedo	13-24% (suburban/urban) +14-15% (rural)

941
 942
 943
 944
 945

946
 947
 948
 949
 950

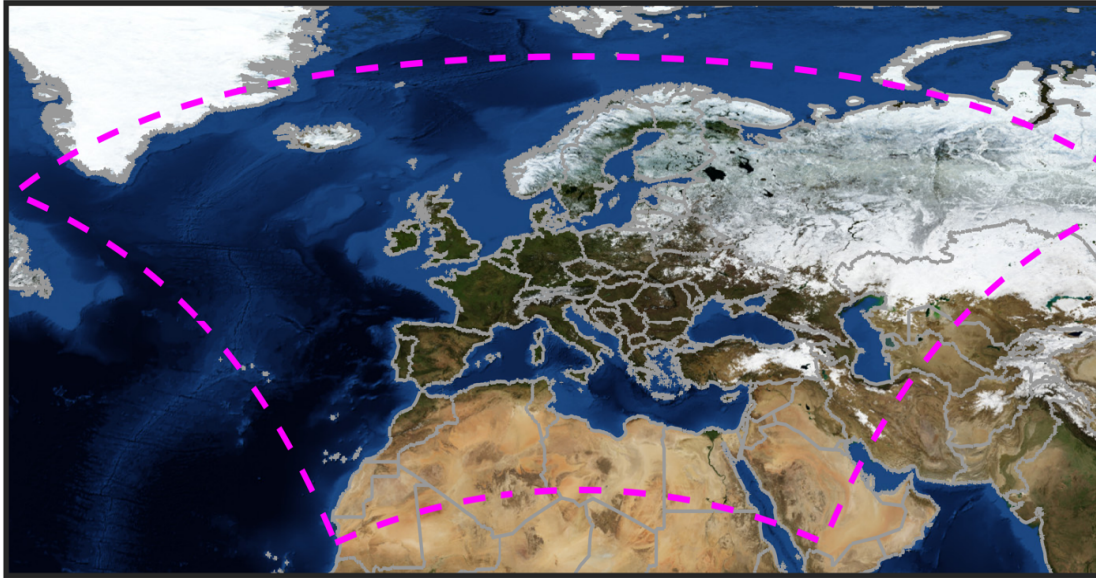
Table 2. Reaction rates relating to the chemical pathways of ozone formation and loss over box L (proximity of central Europe).

Reactions	Production (P) or loss (L)	April 2020 (ppbv/hr)	April 2019 (ppbv/hr)	Net diff ^a (ppbv/hr)
HO ₂ +NO	P	0.85	0.91	-0.06
RO ₂ +NO	P	0.44	0.41	+0.03
NO ₂ +OH	L	0.10	0.14	+0.04
O ¹ D+H ₂ O	L	0.07	0.08	+0.01
O ₃ +VOCs	L	0.01	0.01	0.00
O ₃ +HO _x	L	0.09	0.08	-0.01
J _{NO2} [NO ₂]	P	14.61	27.28	-12.67
k _{NO+O3} [NO][O ₃]	L	15.11	28.52	+13.40
J _{NO2} [NO ₂]- k _{NO+O3} [NO][O ₃]	N/A	-0.50	-1.24	+0.74
Numerically solved PO ₃	N/A	-0.79	-1.53	+0.74

951 ^a A positive net difference indicates higher (lower) production (loss) in 2020 with respect to 2019.
 952

953

CMAQ 15-km Domain

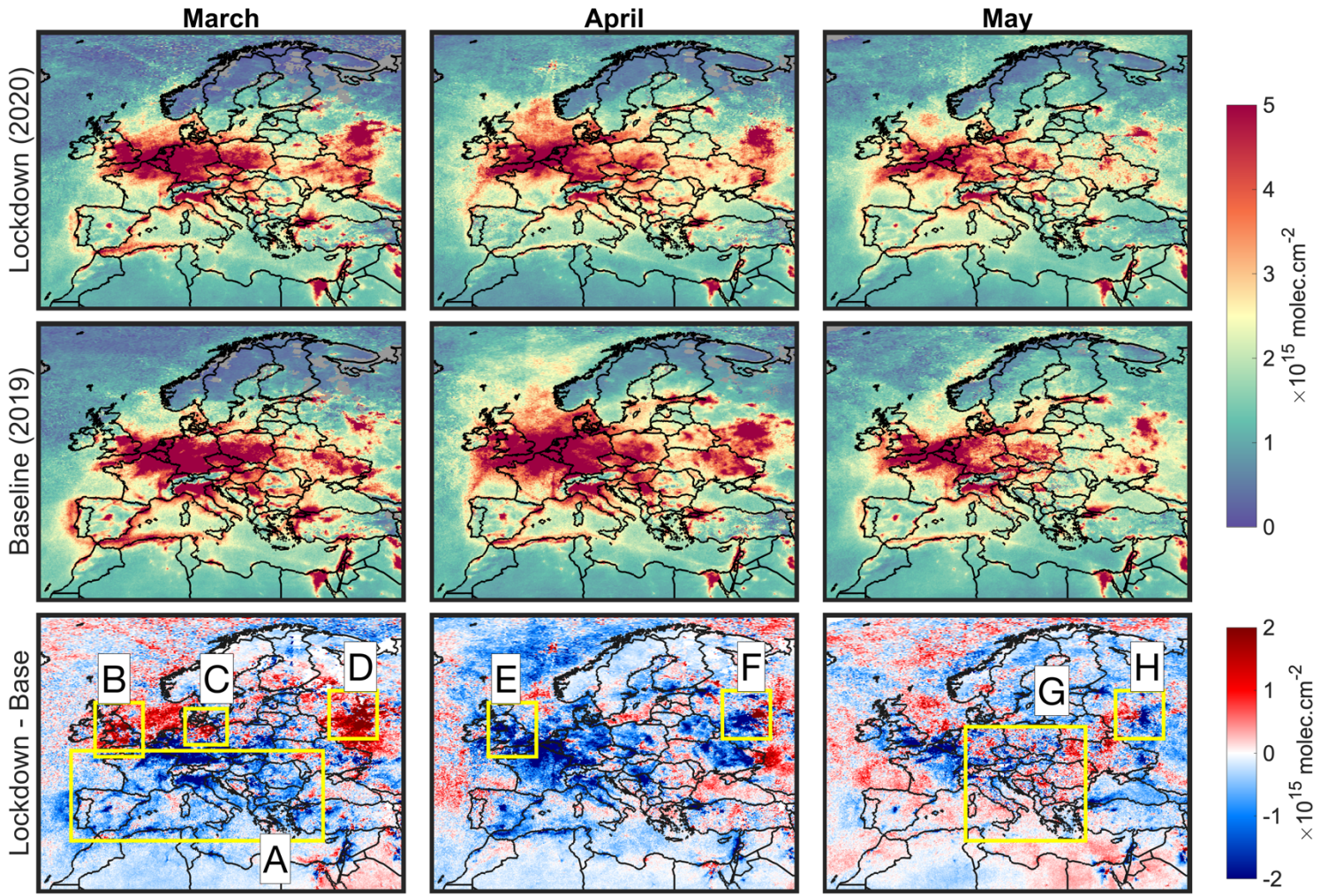


954

955 **Figure 1.** The WRF-CMAQ 15 km domain covering Europe. The background picture is based
956 on the publicly available NASA Blue Marble (© NASA).

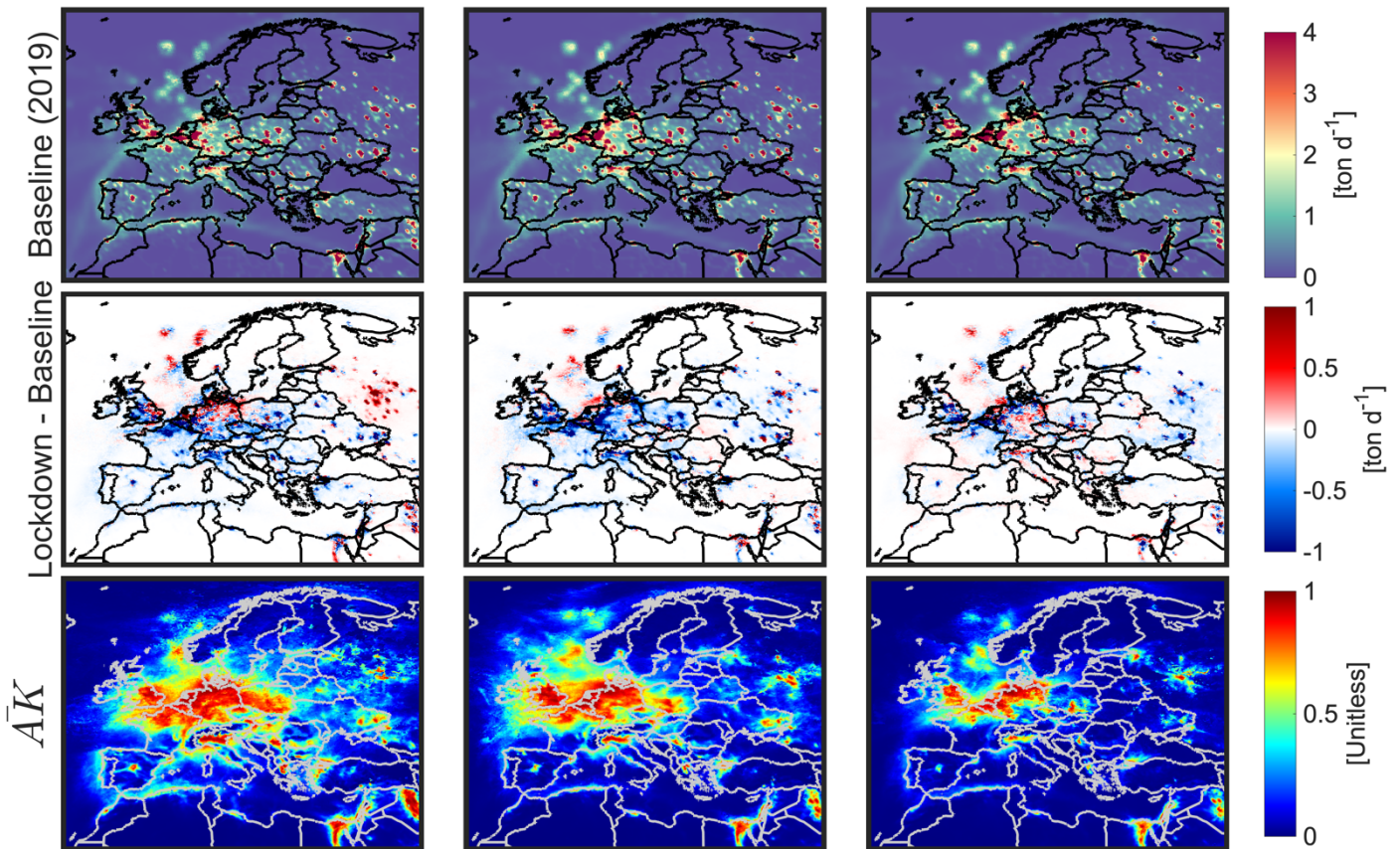
957

958
959



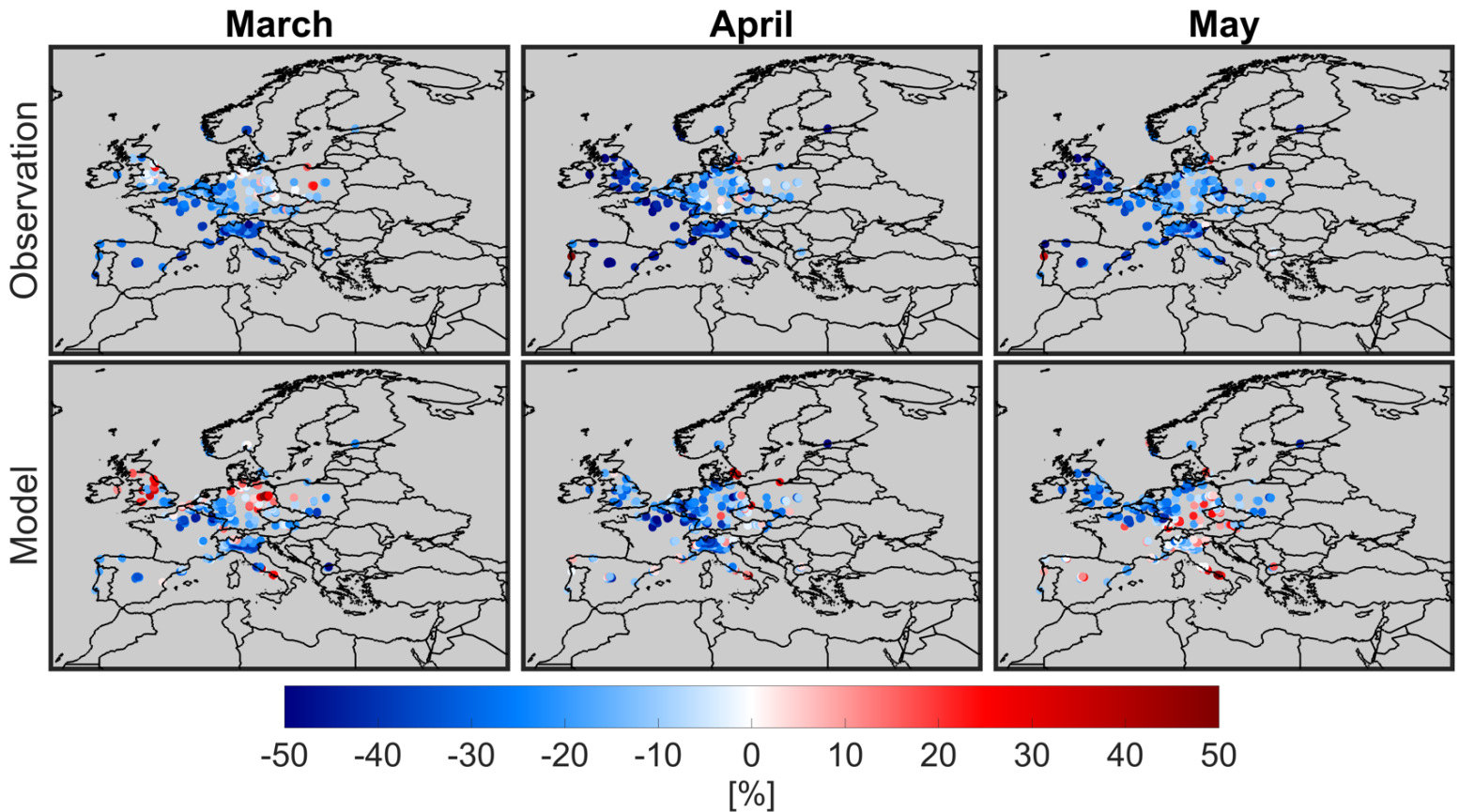
961 **Figure 2.** (first row) Maps of tropospheric NO₂ from the TROPOMI sensor during months of
962 March, April, and May in 2020 (lockdown). (second row) Same as the first row but for the baseline
963 year (2019). (last row), Difference of the columns in 2020 with respect to those of 2019. All
964 columns are corrected for the bias and their AMFs are recalculated iteratively based on the
965 posterior profiles derived from our inverse modeling practice. The satellite-derived columns are
966 subject to errors, so a direct interpretation of their magnitudes cannot be performed in a robust
967 manner.
968

969
970



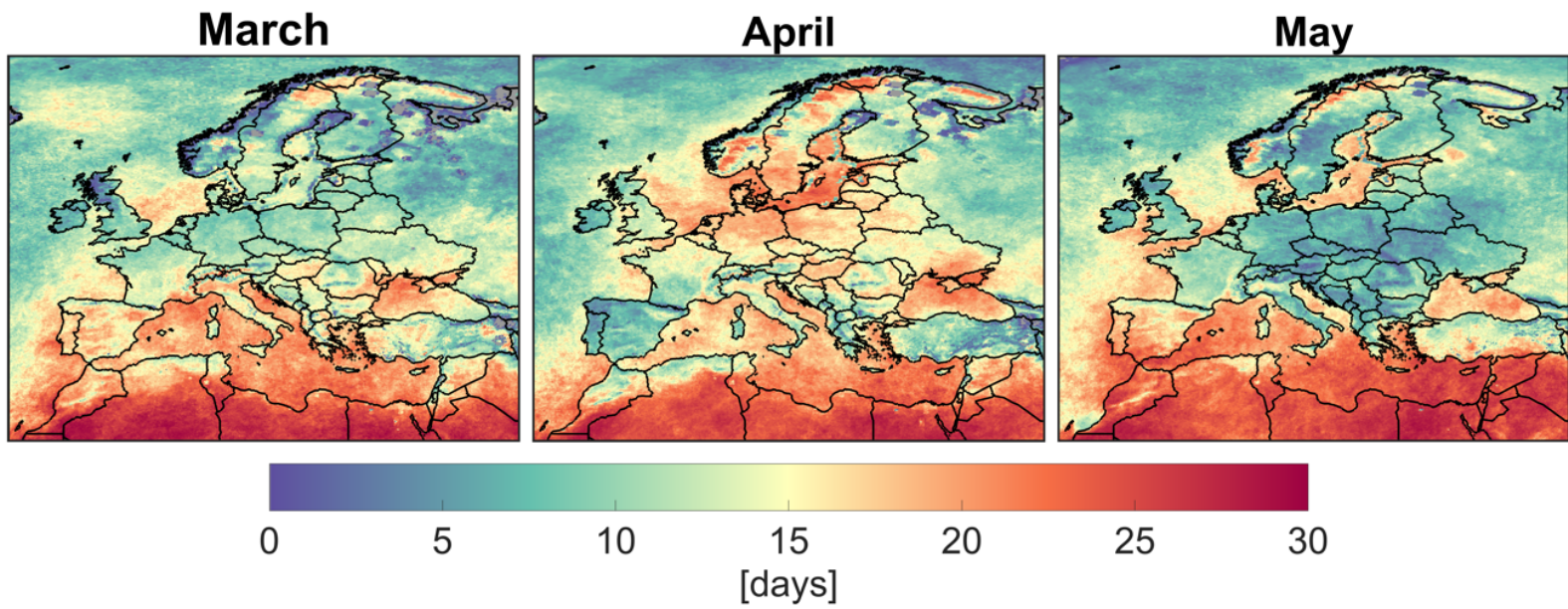
972 **Figure 3.** Top-down estimates of total NO_x during months of March, April and May in 2019
973 (baseline) and the differences between emission in 2020 (lockdown) and 2019. To infer the
974 magnitude of emissions in 2020, the second row should be added to the first one. Both TROPOMI
975 HCHO and NO_2 observations are jointly used to estimate these numbers. Averaging kernels (mean
976 values based on both 2019 and 2020 estimates) describe the level of credibility of the estimate which
977 is heavily dependent on the TROPOMI signal-to-noise ratios.
978

979
980
981
982
983



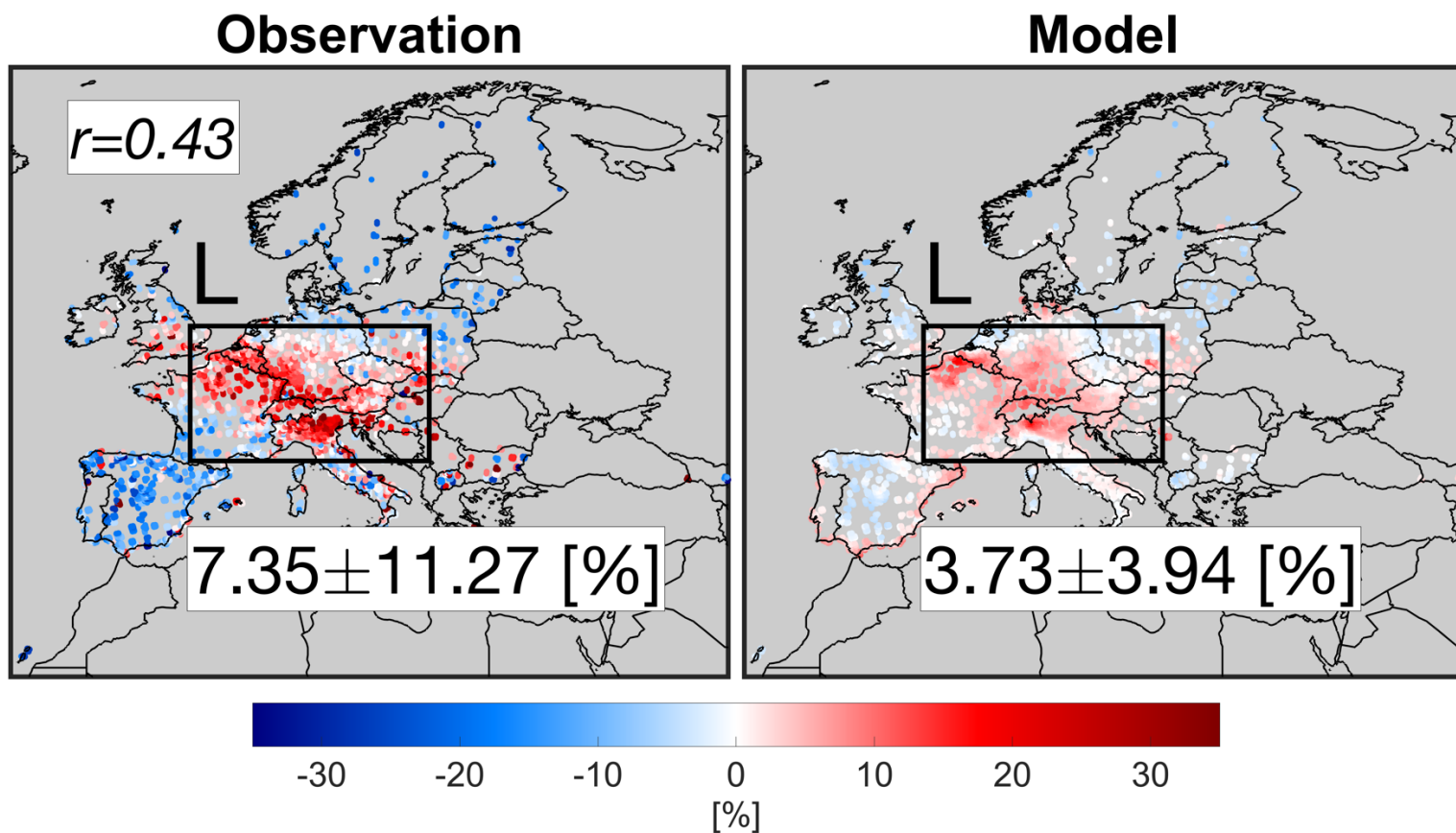
985 **Figure 4.** Scatter maps of relative changes in surface NO₂ concentrations suggested by the
986 European air quality network (first row), and the constrained model (second row). Results are
987 daily-averaged. We only consider grid cells whose averaging kernels (from the NO_x inversion)
988 are above 0.5. Furthermore, grid cells having more than 2 stations are only included to partly
989 account for the spatial representivity factor. Surface concentrations are not accounted for the
990 NO_z family interferences.
991

992
993

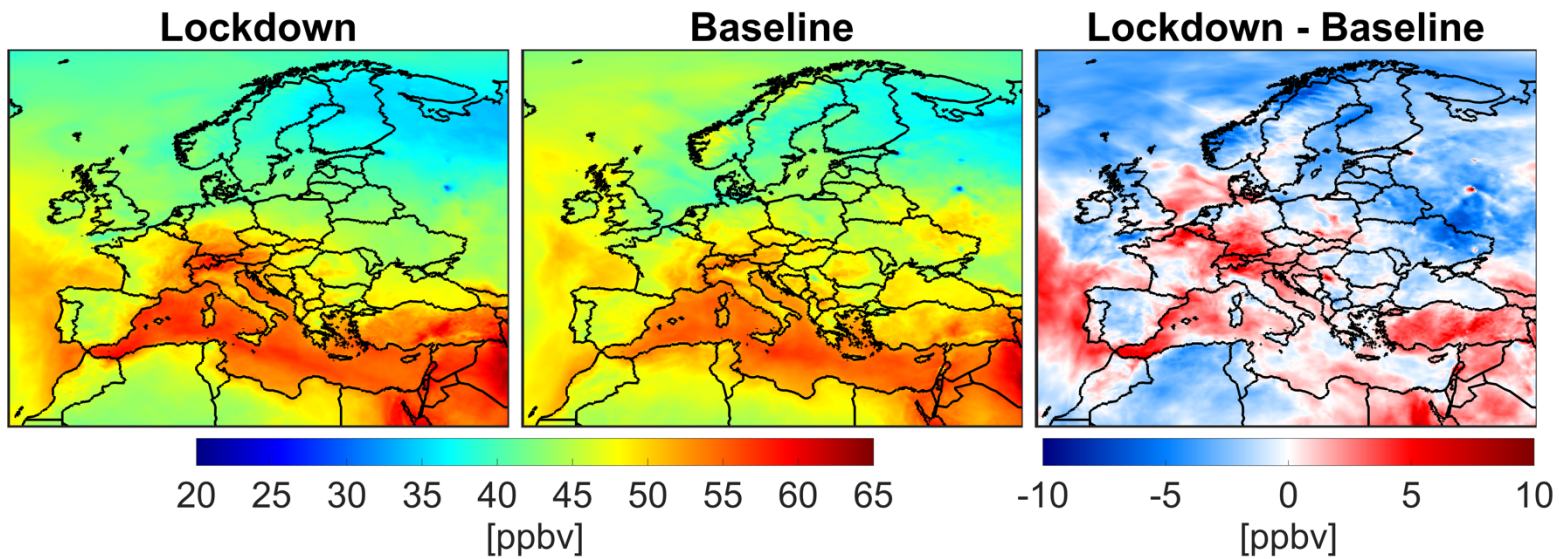


995 **Figure 5.** The average number of good quality ($qa_flag > 0.75$) TROPOMI tropospheric NO₂ days
996 observed at $15 \times 15 \text{ km}^2$ in 2019 and 2020. These numbers are heavily affected by cloudiness.
997

998
999
1000



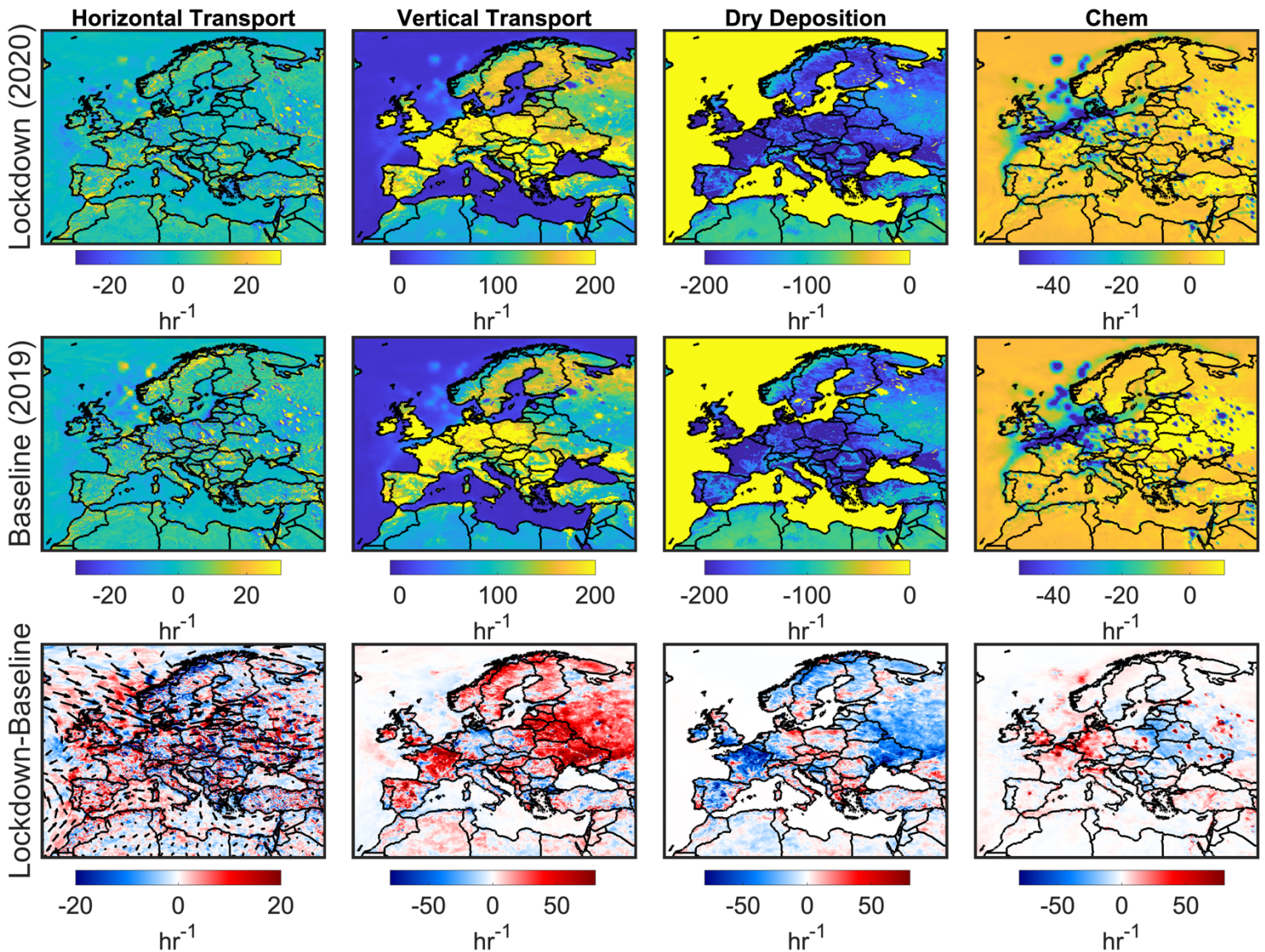
1002 **Figure 6.** Changes in surface MDA8 ozone concentrations suggested by the observation (left),
1003 and the constrained model (right) in April 2020 relative to those in 2019. **The numbers are based**
1004 **on the box L region.**
1005



1007 **Figure 7.** Simulated surface MDA8 ozone concentration using the constrained model in the month
1008 of April 2020 (lockdown), April 2019 (baseline), and their difference.
1009

1010

1011

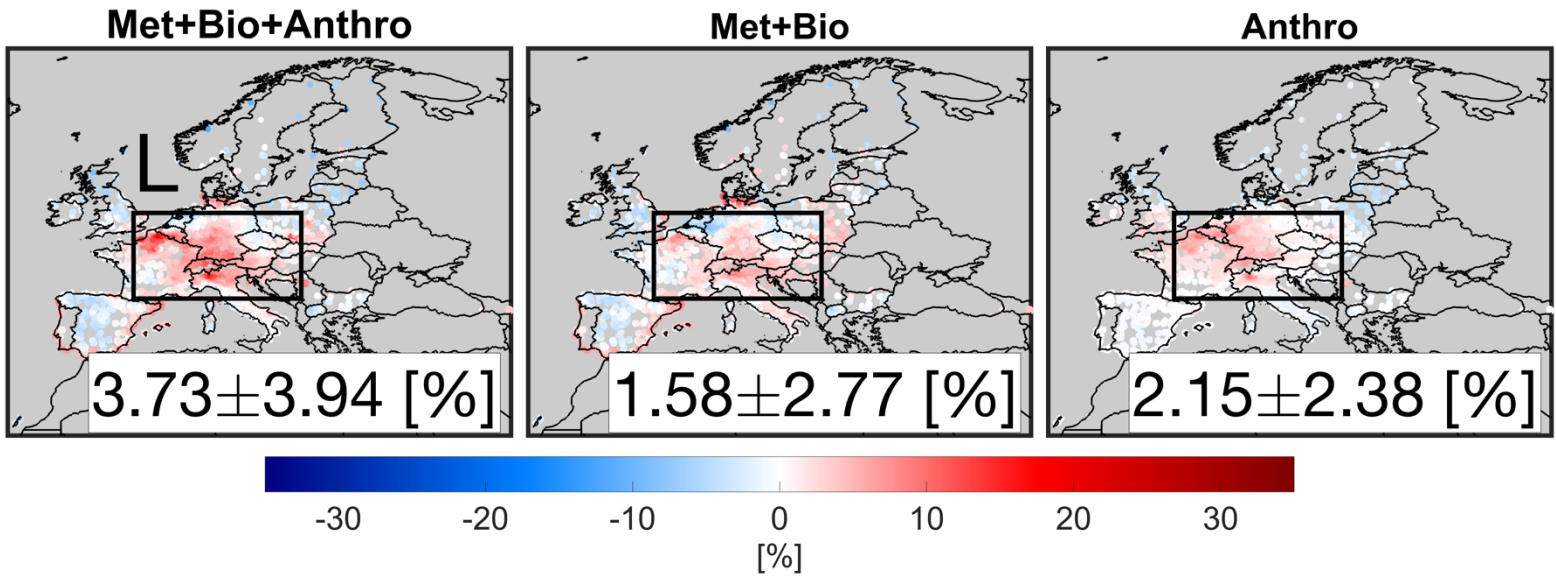


1013 **Figure 8.** Surface process tendencies (hr^{-1}) including horizontal transport (advection plus
1014 diffusion), vertical transport (advection plus diffusion), dry deposition, and chemistry. Positive
1015 (negative) values mean source (sink) of ozone. These outputs are based on the constrained
1016 model. Wind vectors are the difference.

1017

1018

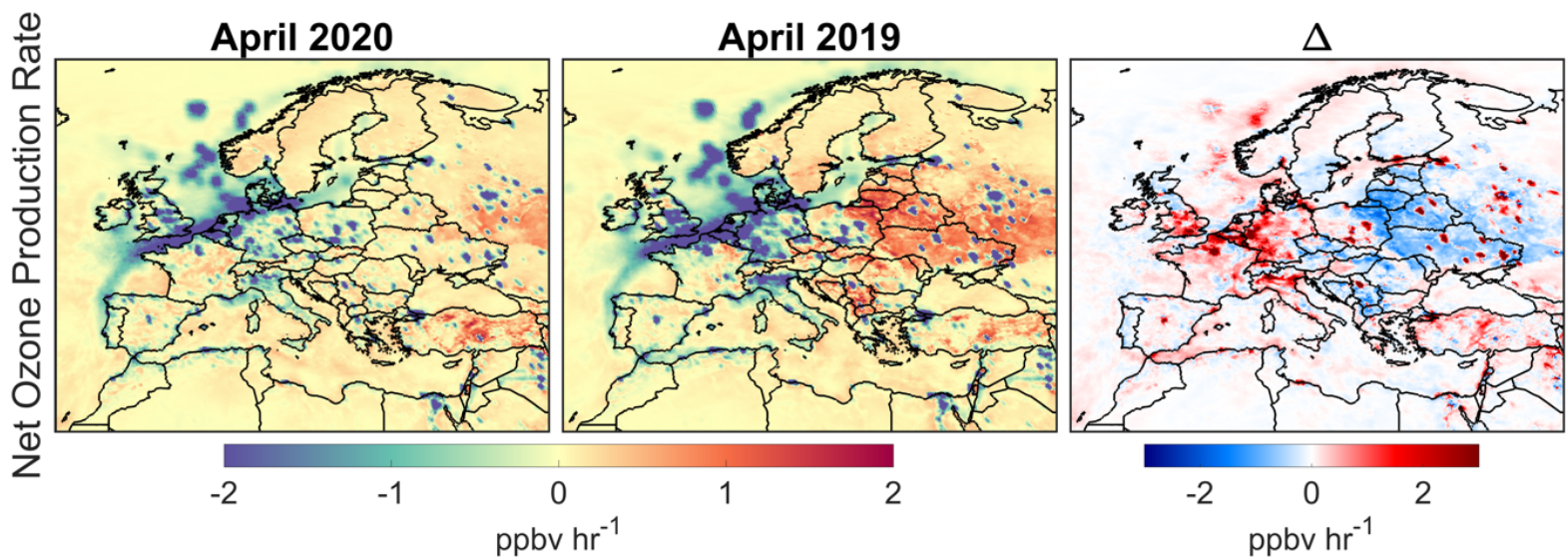
1019
1020
1021



1023 **Figure 9.** Simulated MDA8 surface ozone difference between April 2020 with respect to April
1024 2019 including (left) dynamical meteorology, biogenic and anthropogenic emissions, (middle)
1025 dynamical meteorology and biogenic emissions, and (right) the subtraction of the previous
1026 scenarios isolating dynamical anthropogenic emissions. Emissions used for these experiments
1027 are based on the top-down estimates.
1028
1029

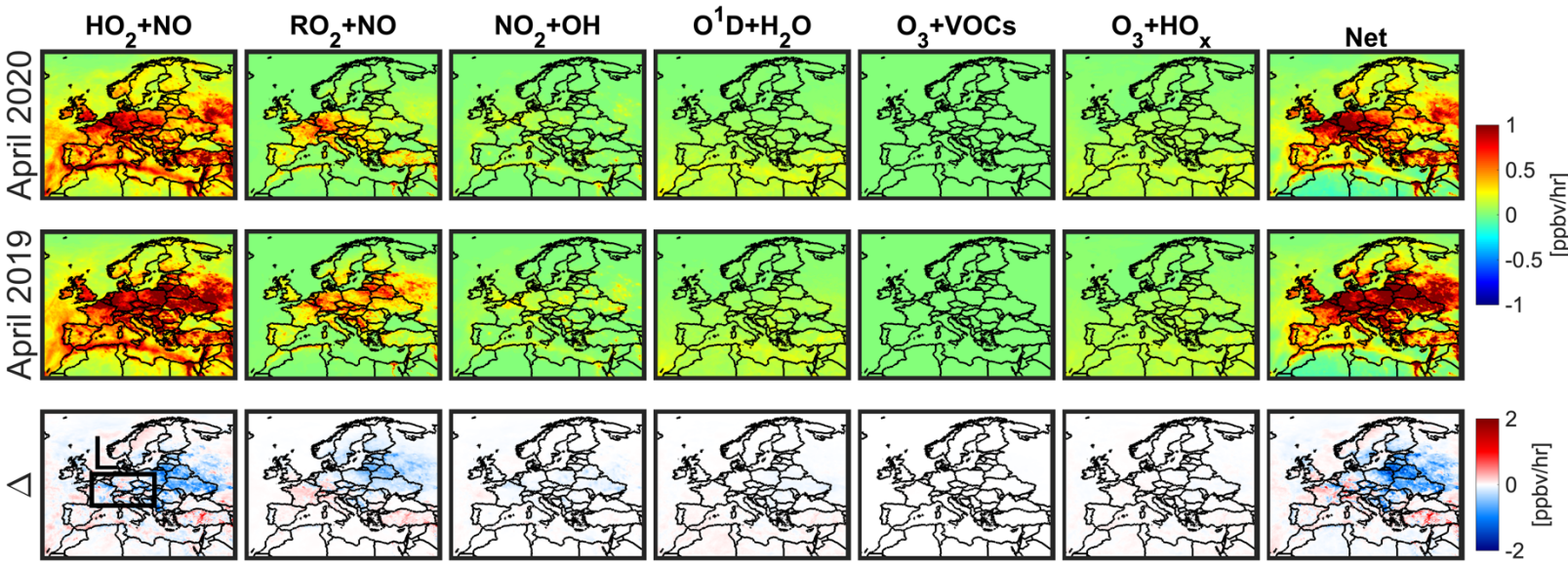
1030

1031

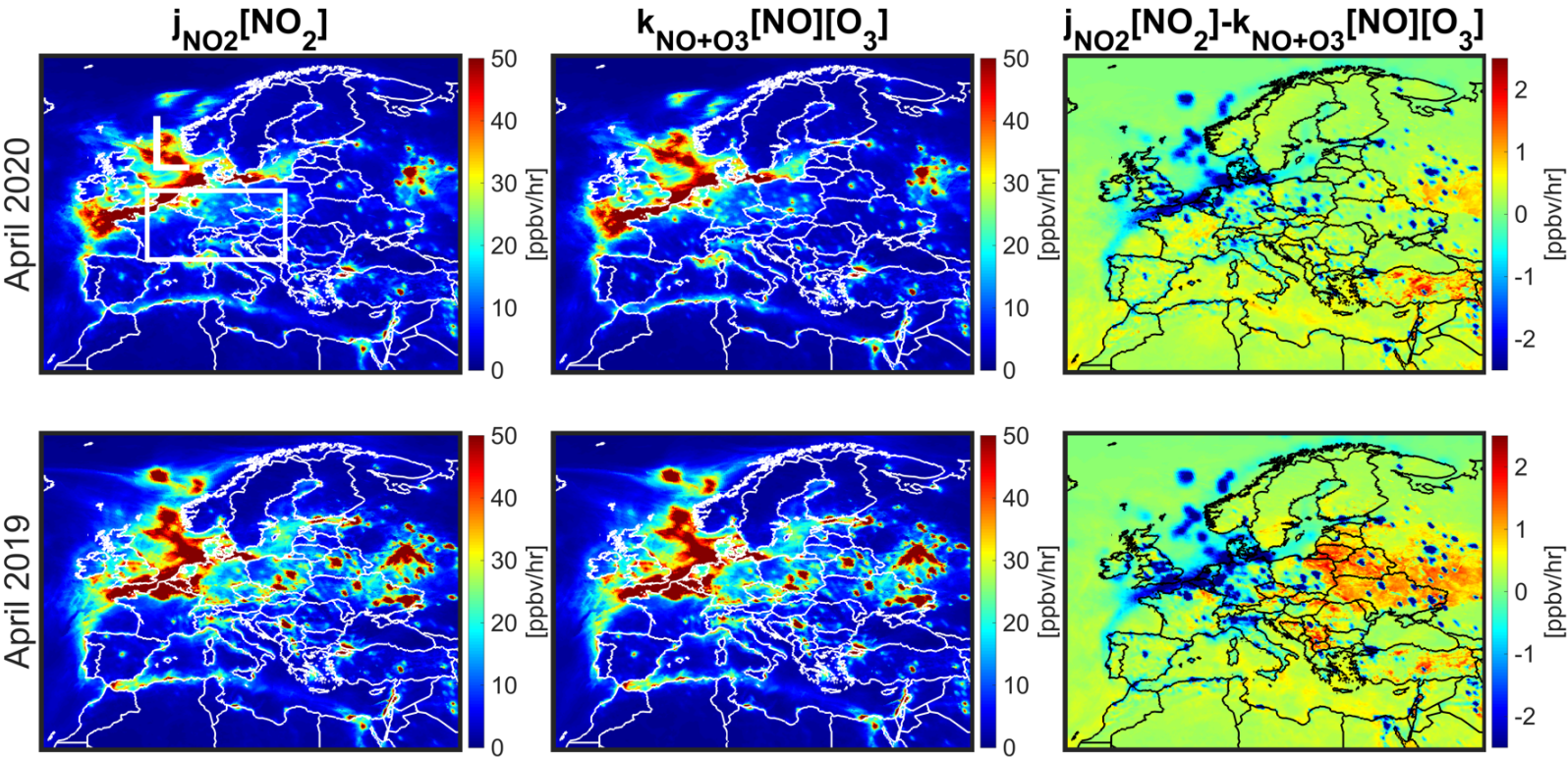


1033 **Figure 10.** Numerically-solved net ozone production rates based on the WRF-CMAQ simulations
1034 using the constrained emissions by the satellite data in April 2020, 2019, and the difference. These
1035 values are over the surface and are averaged during the MDA8 hours.

1036



1038 **Figure 11.** Surface chemical processes involved in equation 5 (ppbv hr^{-1}) pertaining to the
 1039 production and loss of ozone in April 2020 (lockdown) and 2019 (baseline) during MDA8 hours.
 1040 These outputs are based on the constrained model.
 1041



1043 **Figure 12.** Surface chemical processes involved in equation 6 (ppbv hr^{-1}) pertaining to the O_3 -
 1044 NO-NO_2 partitioning in April 2020 and 2019 during MDA8 hours. The constrained model by the
 1045 satellite observations is used to derive these outputs.

1046

1047

1048